ROBUST HIGH-RESOLUTION REDUCED FIELD-OF-VIEW MRI WITH SHEARED 2D RF EXCITATION

A THESIS SUBMITTED TO

THE GRADUATE SCHOOL OF ENGINEERING AND SCIENCE

OF BILKENT UNIVERSITY

IN PARTIAL FULFILLMENT OF THE REQUIREMENTS FOR

THE DEGREE OF

MASTER OF SCIENCE

IN

ELECTRICAL AND ELECTRONICS ENGINEERING

By

Bahadır Alp Barlas

July 2022

Robust High-Resolution Reduced Field-of-View MRI with Sheared 2D RF Excitation
By Bahadır Alp Barlas
July 2022

We certify that we have read this thesis and that in our opinion it is fully adequate, in scope and in quality, as a thesis for the degree of Master of Science.

Emine Ülkü Sarıtaş Çukur(Advisor)

Tolga Çukur

Esin Öztürk Işık

Approved for the Graduate School of Engineering and Science:

Orhan Arıkan
Director of the Graduate School

ABSTRACT

ROBUST HIGH-RESOLUTION REDUCED FIELD-OF-VIEW MRI WITH SHEARED 2D RF EXCITATION

Bahadır Alp Barlas
M.S. in Electrical and Electronics Engineering
Advisor: Emine Ülkü Sarıtaş Çukur
July 2022

Reduced field-of-view (FOV) single-shot echo-planar imaging (ssEPI) is a widely applied imaging technique for diffusion-weighted magnetic resonance imaging (MRI), due to its robustness against in-plane off-resonance artifacts. Two-dimensional echo-planar RF (2D RF) excitation is a popular approach for reduced-FOV imaging due to its fat suppression capability and sharp slab profiles. However, long pulse durations render 2D RF pulses sensitive to through-plane off-resonance effects, causing local signal losses in reduced-FOV images. The standard 2D RF pulses also generate excitation replicas along the slice stack, limiting the slice coverage during multislice imaging. This thesis proposes a sheared 2D RF design for reduced-FOV imaging for significant reduction in pulse duration, leading to significant improvement in through-plane off-resonance robustness. The proposed design also provides unlimited slice coverage and high fidelity fat suppression. Sheared k-space trajectories are designed such that the excitation replicas are positioned outside the slice stack to guarantee unlimited slice coverage, while ensuring identical k-space coverage as that of a standard 2D RF pulse. The efficacy of the sheared design is demonstrated by extensive simulations in terms of pulse duration, fat suppression capability, and signal comparisons under off-resonance effects for a range of design parameters and hardware limits. The sheared and standard 2D RF pulses are then compared via imaging experiments on a custom head and neck phantom, and in vivo imaging experiments in the spinal cord at 3 T. The results show that in regions with high off-resonance effects, the sheared 2D RF pulse improves the signal by more than 50% when compared to the standard 2D RF pulse while preserving profile sharpness. Lastly, the benefits of the sheared design are demonstrated for low-cost low-field MRI systems via simulations and phantom experiments, making reduced-FOV

imaging applicable on these systems. The proposed sheared 2D RF design will be especially beneficial in regions suffering from a variety of off-resonance effects, such as spinal cord and breast.

Keywords: 2D RF pulse, sheared trajectory, reduced field-of-view imaging, off-resonance robustness, fat suppression, multislice imaging.

ÖZET

KESİMLİ 2D RF EKSİTASYON İLE GÜRBÜZ YÜKSEK ÇÖZÜNÜRLÜKLÜ İNDİRGENMİŞ GÖRÜŞ ALANLI MRG

Bahadır Alp Barlas
Elektrik ve Elektronik Mühendisliği, Yüksek Lisans
Tez Danışmanı: Emine Ülkü Sarıtaş Çukur
Temmuz 2022

İndirgenmiş görüş alanlı (GA) tek vuruşlu eko düzlemsel görüntüleme sekansı, rezonans kayması etkilerine karşı olan gürbüzlüğü nedeniyle difüzyon-ağırlıklı manyetik rezonans görüntülemede (MRG) oldukça sık uygulanan bir görüntüleme yöntemidir. İki boyutlu eko düzlemsel RF (2D RF) eksitasyonları ise yağ baskılama kapasitesi ve faz-kodlama yönündeki keskin kesit profilinden kaynaklı olarak indirgenmiş-GA görüntülemede oldukça popüler bir uygulamadır. Fakat, uzun darbe süreleri 2D RF darbelerinin manyetik alan homojensizliklerine karşı olan hassasiyetini artırarak indirgenmiş-GA görüntülerinde yerel sinyal kayıplarına sebebiyet vermektedir. Ek olarak, kesit yönünde beliren kopya eksitasyonlar, görüntüsü alınabilecek kesit sayısı miktarını kısıtlamaktadır. Bu tezde, darbe süresini önemli miktarda azaltmak ve böylece indirgenmiş-GA görüntülemedeki manyetik alan homojensizlik etkilerine karşı olan gürbüzlüğü artırmak için kesimli 2D RF tasarımı önerilmiştir. Önerilen tasarım, ek olarak kesit sayısı sınırını ortadan kaldırmakta ve yüksek oranda yağ baskılama sağlamaktadır. Kesimli eksitasyon k-uzayı gezingesi, standart 2D RF darbesi ile aynı k-uzayı kaplama seviyesini sağlarken, kopya eksitasyonları çoklu kesit alanının dışına konumlandırarak kesit sayısı sınırını ortadan kaldıracak şekilde tasarlanmaktadır. Kesimli tasarımın etkinliği; darbe süresi, yağ baskılama kapasitesi ve manyetik alan homojensizlik etkileri altındaki sinyal kıyaslamaları açısından, farklı tasarım parametreleri ve donanım sınırlamalarında gerçekleştirilen kapsamlı benzetimler ile gösterilmiştir. Ayrıca kesimli ve standart 2D RF darbeleri, gerçekçi bir kafa ve boyun fantomu üzerinde görüntüleme deneyleriyle ve omurilik bölgesinde in vivo deneyler ile 3 T'de kıyaslanmıştır. Elde edilen sonuçlara göre yüksek rezonans kayması etkileri altında kesimli 2D RF darbesi standart 2D RF darbesine kıyasla %50 oranında sinyal miktarını artırmayı

başarırken, profil keskinliğini korumaktadır. Son olarak, kesimli tasarımın düşük maliyetli düşük alanlı MRG sistemlerindeki faydaları, benzetimler ve fantom deneyleri ile gösterilmiş, ve böylece indirgenmiş-GA görüntüleme bu sistemlerde uygulanabilir hale getirilmiştir. Önerilen kesimli 2D RF tasarım yöntemi, omurilik ve meme gibi çeşitli rezonans kayması etkilerine maruz kalan bölgeler için özellikle faydalı olacaktır.

Anahtar sözcükler: 2D RF darbe, kesimli gezinge, indirgenmiş görüş alanlı görüntüleme, rezonans kayması gürbüzlüğü, yağ baskılama, çoklu kesit görüntüleme.

Acknowledgement

My undergraduate experience led me to develop an interest in signal and image processing, and optimization techniques which eventually turned into a passion to pursue my career in the academia. Although I had no experience in medical imaging, I found myself in an outstanding research environment developing novel acquisition and reconstruction techniques for MRI. Looking back at these three years, I am very grateful that I have chosen the medical imaging field as a research focus. Even though there were tough times, I have experienced one of my best periods in life. Thus, I would like to thank the people I owe for this amazing and unmatched experience which significantly contributed to my academic and personal self-growth.

Before I start, I would like to thank Scientific and Technological Research Council of Turkey (TUBITAK Grant No: 117E116) for its support to this thesis.

First of all, I would like to thank Dr. Emine Ülkü Sarıtaş, who has been an excellent supervisor to me, for her invaluable support. Even though I was very hesitant and pessimistic to ask to join her group for MSc due to the lack of experience I had in medical imaging and the fact that we hadn't met during my undergraduate years; she was very encouraging towards me by stating that I could be successful in this field while also mentioning the challenges that I will face. At the end of my MSc period, I am still surprised by the accuracy of her predictions. Of course, this wouldn't be possible without her immense effort, patience and tolerance. She answered even the most ridiculous questions I asked with kindness and importance and preserved her attitude even when I was incredibly stubborn. I still can't believe how many times she explained the theory of 2D excitation pulses. Even in the hectic times, she somehow manages to spend many hours on my research, forsaking her already limited free time. During these times, she could detect and resolve my lack of knowledge. Furthermore, it was also such a pleasure to have non-academic conversations with her due to her modest but objective and complex reasoning. I can not thank her enough for her effort and patience, and I hope that I will carry the responsibility that her effort deserves.

Through these three years, I had an opportunity to meet with a group of wonderful people. Elif is one of the kindest, most helpful, and most elegant people I have ever met. I can't count how often she helped me without hesitation, even if she was swamped. Although there were many times that I made her upset due to my stubbornness, she continued to be very forgiving and kind. I am very grateful that I have met with her, and I hope that one day her hatred towards peanut "butter" caused by my irrational passion for debate will disappear. I am very fortunate to meet with Abdallah, who shares similar interests. I will miss our ritual where we have long conversations while walking around. I also miss the quality time I spent with Aslı, one of the nicest and friendliest people. Although I was a bit nervous, her aura eliminated my negative emotions when I talked with her. I also want to thank Abdallah and Aslı for their significant support during my research. Even though we didn't have a chance to spend more time due to the pandemic, Mustafa had always found a way to help. Even after his graduation, he still manages to support his colleagues. I would like to thank Tunç, Beril, Alper, Sefa, and Salman for their kindness and support. I would also thank my friends for years, Alp, Gökberk, Mahmut, and Onurcan. I have enjoyed the traditional gaming sessions where Mahmut, Onurcan, Furkan, and I compete with each other.

I would also like to thank my grandmothers, Elmas and Zehra, and my grandfather, Yüksel. Although he could be seen as unambitious, my grandfather, Yüksel, was continuously improving the summerhouse all by himself to provide his family with a relaxed and peaceful environment until the last seconds of his life. Even in the presence of the most complicated issues, he has always encouraged me to be motivated and positive, and I really admire how he was sincerely optimistic about life. I thank my grandmother, Zehra, for always being supportive and thoughtful. Even though she gets upset when we discuss politics, she always manages to stay calm and tolerate my stubbornness. My grandmother, Elmas, fills a special place in me. Although she was forced to leave school early on, I have never seen a person with greater insight. Still today, I am surprised by how objective, and just she is to the people and events. Although I am determined, I can only hope to achieve the same capability.

Finally, I would like to thank my family for their unconditional support. My brother, Bora, who is four years smaller than me, is always by my side with his joy and uniqueness. Despite our distinct personas, our clear understanding of each other shows our powerful bond. It is a pleasure to talk with him about stupidly ridiculous topics for many hours after a tiresome period. He is not only an excellent brother but also a great friend. Recalling the earliest moments in my memory, my parents have always valued my individuality. Thanks to them, I have determined that I had an immense passion for technical problem-solving at a very early age. Accordingly, they encouraged me to look into different branches of engineering by scheduling meetings with the corresponding fields. With their unforced support, I could not find the excellent research environment that I am currently in. Particularly, I could not finish my thesis without the enormous help and patience of my mother, Nilgün. Whenever I struggle, she tries her best to find a solution hoping to reduce my stress. Similar to the case of my brother, I always enjoyed the intellectual debates with my father. Although we are both extremely stubborn and annoying in these debates, these practices significantly developed my self-growth. Overall, I am grateful to my father for doing his best to improve me. Lastly, I would like to thank my cat, PC, for his patience, thoughtfulness, and understanding. He was my greatest companion when I was working on my thesis.

Contents

List of Figures

Chapter 1

Introduction

Diffusion-weighted imaging (DWI) provides a powerful tool for diagnosing conditions related to the pathological changes in tissue microstructure [1, 2]. Although DWI gained its popularity due to its capability of early detection of brain ischemia and cancer [3, 4, 5, 6], it has found a wide range of clinical usage outside the central nervous system for abdominal tissues and organs such as the breast, prostate, and endometrium [7, 8, 9, 10, 11]. Single-shot echo-planar imaging (ssEPI) is by far the most commonly used imaging sequence in DWI because of its speed and robustness against motion-induced artifacts, despite the associated off-resonance distortions [2, 12]. Multishot techniques such as readout-segmented (RS) EPI [13, 14, 15], short-axis propeller (SAP) EPI [16], and interleaved EPI [17, 18, 19, 20] were developed to reduce echo train while keeping the number of shots limited in order to constrain both off-resonance and motion-induced artifacts. In addition, reduced field-of-view (FOV) ssEPI has been proposed to improve in-plane off-resonance robustness by limiting the FOV along the phase-encoding (PE) direction, enabling a significant reduction in the number of PE lines without causing aliasing artifacts [21, 22, 23, 24]. Applications of reduced-FOV techniques such as outer volume suppression [22] reinforced with parallel imaging [25, 26], zoonal oblique multislice (ZOOM) EPI [27, 28], and two-dimensional echo-planar RF (2D RF) pulse excitation [23, 29] together with several combinations of the provided reduced-FOV techniques [30] have been demonstrated successfully in various regions. In particular, due to its fat suppression capability and sharp slab profile features [23], reduced-FOV imaging with 2D RF pulse excitation has been widely applied in regions that typically suffer from off-resonance artifacts such as the spinal cord, prostate, and breast [6, 8, 9, 31, 32, 33].

Despite the improved robustness provided by 2D RF based reduced-FOV ssEPI against in-plane off-resonance distortions, several issues still need to be addressed. Firstly, traversing the excitation k-space in 2D requires longer pulse durations, which in turn increases through-plane off-resonance sensitivity. This sensitivity can cause regions with large susceptibility differences to suffer from a signal loss [23]. Furthermore, 2D RF excitations generate replicas along the blipped (i.e., discretely sampled) axis. Assigning the blipped axis as the slice-selection (SS) axis grants important advantages to this technique, such as inherent fat suppression capability and sharp slab profiles. However, as a trade-off, this assignment limits the slice coverage during multislice imaging, since any overlap between the replicas and the prescribed slice stack causes a significant signal loss due to partial saturation effects. While one can adjust the design parameters to extend the distance between the replicas, the resulting 2D RF pulses have even longer durations, further increasing the aforementioned off-resonance sensitivity [23].

One approach to enhance through-plane off-resonance robustness is adaptive 2D RF pulse design using a B_0 field map acquired prior to imaging [34]. Although this technique successfully reduces the off-resonance-based artifacts without compromising from RF pulse performance, the need to obtain an additional B_0 field map and to redesign a new 2D RF pulse for each subject and each region of interest (ROI) reduces the feasibility of this technique in clinical settings. Another approach is the usage of a second-order shim gradient (Z2) together with a spatial-spectral RF pulse to excite a disk-shaped reduced FOV [35, 36]. While this method achieved a reduction in pulse duration, the low strength of Z2 gradient in commercial MRI systems limits its performance. Previously, two different tilted 2D RF pulse designs were proposed to reposition the replicas along a tilted axis via rotating the excitation k-space trajectory [37, 24]. One of these techniques assigned the blipped axis as the PE-axis, and prioritized pulse duration reduction to enhance off-resonance robustness without considering the fat suppression capability as a criterion [37]. The second technique assigned the blipped axis as the SS-axis, providing unlimited slice coverage together with robust fat suppression, without any improvement in off-resonance robustness [24]. This second technique has been successfully applied in various target regions such as the pancreas and prostate [38, 39].

In this thesis, a sheared 2D RF pulse design is proposed to achieve a significant improvement in through-plane off-resonance robustness by decreasing the pulse duration through a sheared coverage of the excitation k-space. The proposed technique further provides unlimited slice coverage while preserving profile sharpness and fat suppression capability. The sheared and standard 2D RF pulses are compared via extensive simulations, including analyses on pulse duration, profile sharpness, fat suppression capability, and signal comparison under off-resonance effects. In addition, phantom experiments in a custom head and neck phantom and in vivo imaging experiments in the spinal cord at 3 T are presented to compare full-FOV ssEPI images and reduced-FOV ssEPI images with the sheared and standard 2D RF pulses. The results show that the sheared 2D RF design achieves reduced pulse durations and high fidelity fat suppression for a wide range of design parameters needed for reduced-FOV imaging, as well as a wide range of scanner hardware limits. Furthermore, the proposed technique accomplishes significant improvement in the off-resonance robustness, demonstrating reduced-FOV images with increased signal levels especially in regions that suffer from high off-resonance effects. Lastly, the proof-of-concept applicability of the sheared 2D RF design is demonstrated for reduced-FOV imaging in low-cost low-field MRI systems, where hardware limitations prevent the applicability of numerous MRI techniques. Accordingly, extensive simulations and phantom experiments in a custom head and neck phantom are conducted for the hardware limits of low-cost 0.35 T and 1.5 T MRI scanners. The results show that the sheared 2D RF design can make reduced-FOV imaging applicable on these systems, by providing reduced pulse durations and increased off-resonance robustness.

Chapter 2

Background and Theory

2.1 Single-shot Echo-Planar Imaging for Diffusion Weighted Imaging

DWI is a powerful non-invasive tool that provides characterization and measurement of the diffusion in the tissue microstructure [1, 2, 40]. DWI can detect pathological changes in the tissues, allowing early diagnosis of ischemic stroke, brain ischemia and cancer, even surpassing computerized tomography (CT) in terms of early detection performance [3, 4, 5, 6]. Consequently, DWI gained enormous popularity in the clinical settings and is also applied in a wide range of target regions outside the central nervous system [7, 8, 9, 10, 11]. However, since diffusion is a measure of microscopic displacement by definition, DWI is sensitive to bulk motion that is mainly caused by natural factors such as breathing and swallowing. Any significant motion during diffusion-sensitizing gradients causes phase errors and shifts in the corresponding k-space data. Furthermore, these motion-induced phase errors and shifts differ for each repetition time (TR), leading to ghosting artifacts in the images, as well as miscalculation of diffusion coefficients [41].

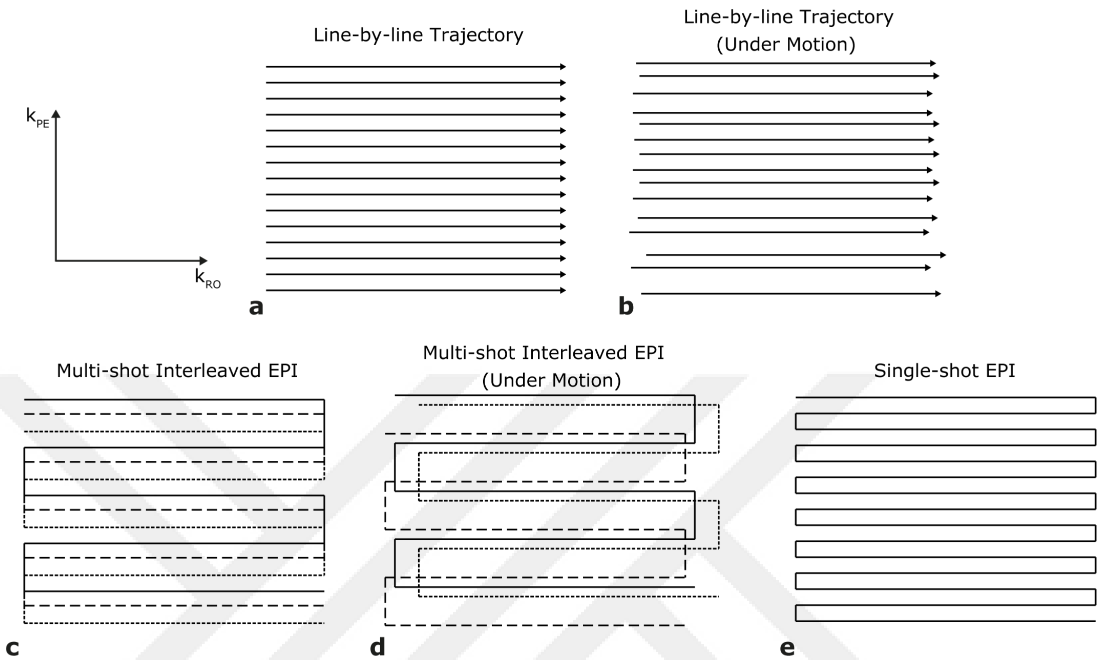

Figure 2.1: *The effects of bulk motion during diffusion-sensitizing gradients. A line-by-line k-space trajectory (a) without and (b) with motion are shown. Since k-space lines are acquired one by one at each TR, they are exposed to independent and unknown phase errors and shifts. Multi-shot interleaved EPI trajectory (c) without and (d) with motion are shown. The k-space lines acquired within the same shot experience the same phase error and shift, generating a consistency within each shot. Nonetheless, the inconsistency still occurs among the lines of different shots. (e) ssEPI covers the entirety of the targeted k-space region in a single shot, causing all k-space lines to experience identical phase error and shift.*

Figure 2.1 shows the effects of bulk motion during diffusion-sensitizing gradients on three different acquisition schemes: a line-by-line trajectory, multi-shot interleaved EPI, and single-shot EPI (ssEPI). The k-space lines are acquired one by one at each TR in the line-by-line trajectory. However, since bulk motion can be different for each TR, the k-space lines experience phase errors and shifts of unknown amounts, as shown in Fig. 2.1b. This inconsistency between the k-space lines causes severe ghosting artifacts in the DWI image. Multi-shot interleaved EPI is an alternative technique, where multiple k-space lines are acquired during each TR, allowing to acquire the whole target k-space region within a few shots.

Figure 2.1c shows a sample three-shot interleaved EPI sequence. As shown in Fig. 2.1d, for the case of bulk motion, although the k-space lines acquired within a given shot shift together, the shifts for different shots are different. Again, these shifts cause an inconsistency among the k-space lines in the overall acquisition. On the other hand, ssEPI covers the entirety of the targeted k-space region in a single shot. Therefore, under the influence of bulk motion, all k-space lines shift by the same amount, preventing potential inconsistencies in the data acquisition.

Due to its robustness against motion-induced artifacts and its speed, ssEPI is still one of the most commonly used acquisition techniques in DWI. However, covering the whole k-space in a single shot raises trade-offs to consider. In MRI, the field-of-view (FOV) must be chosen larger than the excited anatomy to prevent aliasing artifacts, where tissues of different regions overlap with each other. Since k-space is sampled discretely along the phase-encode (PE) direction, the distance between consecutive k-space lines must be small enough to support a sufficiently large FOV along the PE-direction (FOV_{PE}). Furthermore, high-resolution imaging dictates a sufficiently wide coverage of the k-space, requiring a large number of k-space lines (N_{lines}) to be acquired. Since the entire k-space data is acquired in a single shot in ssEPI, high-resolution imaging of a large FOV_{PE} requires extremely long readout durations. In return, long readout times cause ssEPI to suffer from severe T_2^* decay during data acquisition, leading to blurring along the PE-direction of the images. Furthermore, the time interval between two consecutive k-space lines, i.e., echo-spacing, T_{ESP}, is long for ssEPI, which causes in-plane off-resonance sensitivity. The off-resonance effects cause accumulated phase-errors during the acquisition, leading to a position-dependent shift along the PE-direction in ssEPI images [21]. This shift can be expressed as [42]:

$$\Delta y = \Delta f \, T_{ESP} \, FOV_{PE} \tag{2.1}$$

Here, Δf is the off-resonance frequency. Note that Eq. 2.1 is also valid for fat signal for $\Delta f = \Delta f_{cs}$, implying that fat experiences undesired shifts along the PE-direction, which leads to a misalignment of water and fat tissues in ssEPI images. Considering the large T_{ESP} of the ssEPI trajectory, this misalignment can be significantly large. Therefore, additional fat suppression methods must be utilized to prevent chemical shift artifacts in ssEPI images.

Different acquisition schemes and techniques have been proposed as an alternative to ssEPI for DWI to obtain sequences with high robustness against motion-induced artifacts with relatively short readout durations. Multi-shot interleaved EPI techniques utilized navigator echos, where the central k-space lines were acquired in addition to the interleaved lines at each shot. Then, the data obtained from the navigator echos were used to estimate and resolve the motion-induced phase errors and shifts [17, 18, 19, 20]. Another multi-shot technique called readout-segmented (RS) EPI was proposed to cover the k-space in segments that split the k-space coverage along the readout direction. This approach allows the segments in each shot to be fully sampled along PE-direction without the expense of long readout durations. Since each segment is sampled at the full Nyquist rate along PE-direction, motion correction with navigator echos does not leave any gaps in k-space data, avoiding potential ghosting artifacts. Additionally, since k-space is acquired piece by piece, the total readout time is significantly shorter than that of ssEPI. Still, RS-EPI has the disadvantage of requiring a navigator echo. Furthermore, splitting the k-space lines to smaller pieces causes inefficient utilization of the gradient strength, which slightly increases the total readout time compared to its multi-shot interleaved EPI counterpart [13, 14, 15].

2.2 Reduced Field-of-View Imaging

Previously, the trade-offs in ssEPI are discussed by emphasizing the importance of supporting a sufficiently large FOV_{PE} to prevent aliasing artifacts in the images. Achieving a high resolution for a large FOV_{PE} requires increasing N_{lines}, leading to a longer readout time. In addition to large N_{lines}, long T_{ESP} needed for high resolution further increases the readout time, causing ssEPI images to suffer from in-plane off-resonance sensitivity as formularized in Eq. 2.1. To address this issue, reduced-FOV ssEPI has been proposed to excite only the region of interest (ROI) along the PE-direction, limiting the slab thickness based on the ROI size [21].

With this approach, FOV_{PE} can be reduced to the size of ROI, which allows extending the distance between consecutive k-space lines. Accordingly, N_{lines} can be decreased for a fixed resolution, allowing a shorter readout duration. With this approach, image quality and in-plane off-resonance robustness can be significantly improved without introducing aliasing artifacts. This advantage can be verified in Eq. 2.1, where reducing FOV_{PE} directly decreases the off-resonance-induced shifts, improving the in-plane off-resonance robustness of ssEPI.

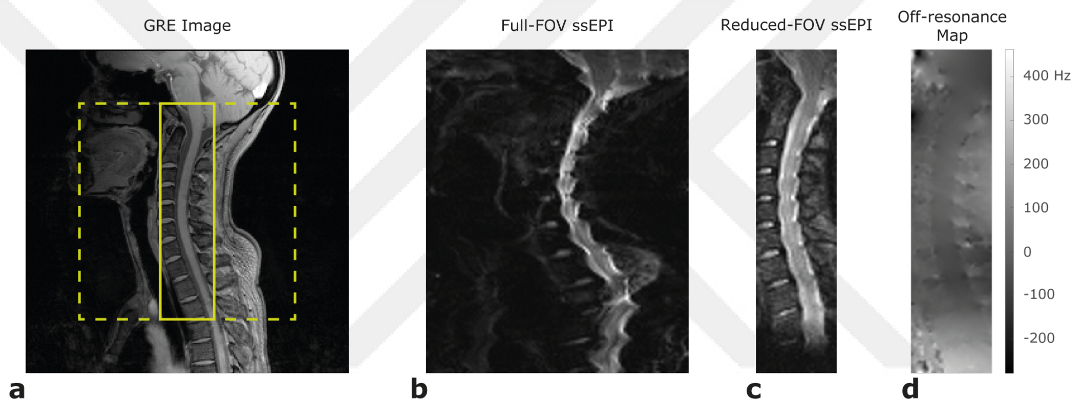

Figure 2.2: *Comparison between full-FOV and reduced-FOV ssEPI via in vivo imaging results in the cervical spine. (a) The image from the double-echo gradient echo (GRE) sequence shows the anatomy together with the full-FOV (yellow dashed rectangle) and reduced-FOV (yellow solid rectangle) regions marked for reference. (b) The full-FOV ssEPI image, acquired using a 1D RF pulse with additional frequency-selective fat suppression, suffer from severe in-plane off-resonance distortions, especially in the regions with high B_0 inhomogeniety. (c) In contrast, the reduced-FOV ssEPI image demonstrates high-resolution and reduced in-plane distortions. (d) The corresponding off-resonance field map shows high off-resonance effects across the cervical spine.*

A performance comparison of full-FOV and reduced-FOV ssEPI is exemplified in Fig. 2.2 for the case of cervical spinal cord imaging. Here, the anatomical, full-FOV ssEPI, and reduced-FOV ssEPI images are shown together with the corresponding off-resonance map. In order to image the cervical spine, full-FOV ssEPI requires a large FOV_{PE} (dashed yellow rectangle) to avoid aliasing artifacts, while a relatively small ROI can be targeted with reduced-FOV ssEPI (solid yellow rectangle). The full-FOV ssEPI is acquired using a 1D RF pulse with additional frequency-selective fat suppression. This image suffers from severe in-plane off-resonance distortions, especially in the central part of the cervical spine, which is typically exposed to high off-resonance effects. In contrast, the reduced-FOV ssEPI image demonstrates high-resolution with reduced in-plane distortions.

Numerous approaches have been proposed for reduced-FOV imaging. One application was to utilize outer volume suppression (OVS) pulses in order to restrain the excitation FOV. In this method, the outer volume regions were excited and then exposed to dephasing gradients. Immediately after this, excitation pulses of the ssEPI sequence were applied, preventing the outer volume regions to recover [22, 43]. Several approaches combined reduced-FOV imaging via OVS and a parallel imaging technique at relatively low acceleration rates for further reduction in the FOV, providing a significant overall reduction in the readout duration. Note that with this way, FOV can be significantly reduced without the expense of high g-factor [25, 26]. Zoonal oblique multislice (ZOOM) EPI technique utilizes a 180° refocusing RF pulse that is selective in the PE-direction. After the entire volume is excited, the refocusing 180° RF pulse suppresses the outer volume of the targeted reduced-FOV region [27, 28]. In contrast to these techniques where additional pulses are utilized to suppress the outer volume, reduced-FOV imaging with 2D RF excitation was proposed to excite only the targeted volume in the first place [23, 29]. Echo-planar trajectory for the excitation k-space requires one axis to be assigned as the blipped (i.e., slow) axis, along which excitation replicas appear due to the discrete sampling in this direction. When the blipped axis is assigned along the SS-direction, water and fat profiles can be fully separated due to the long 2D RF pulse duration, allowing the usage of a 180° refocusing RF pulse to suppress fat signal [23]. This technique has been widely applied in the regions that suffer from extensive fat signal such as the spinal cord, prostate, and breast [6, 8, 9, 31, 32, 33]. Note that these regions also experience high B_0 field inhomogenieties signifying the importance of using a reduced-FOV imaging technique. Despite its advantages, since the excitation replicas are generated along the SS-direction, partial saturation effects can cause severe signal loss if a large number of slices are acquired during multislice imaging. Furthermore, the long duration of the 2D RF pulse makes this method sensitive to through plane off-resonance effects.

2.3 Standard 2D Echo-Planar RF Pulse Design

Standard 2D RF pulses enable independent design of slice profile along SS-axis and slab profile along PE-axis. In this thesis, the fast and blipped directions of the echo-planar k-space trajectory correspond to PE- and SS-axes, respectively (see Fig. 2.3a-b). The corresponding 2D excitation profile features replicas and a relative shift of the fat profile, both along the blipped SS-direction as seen in Fig. 2.3c. In a spin echo sequence, both fat and the replicas can be suppressed using a 180° refocusing RF pulse selective in the SS-axis. Under the small tip angle approximation, a standard 2D RF pulse can be designed as follows [44, 45]:

$$B_1(t) = C_1(\alpha)\, W(k_{SS}(t), k_{PE}(t))\, \|\boldsymbol{G}(t)\|_2 \tag{2.2}$$

Here, $k_{SS}(t)$ and $k_{PE}(t)$ are the SS and PE components of the k-space trajectory, respectively. $C_1(\alpha)$ is a constant that adjusts the flip angle α, W is the excitation k-space weighting to achieve the desired 2D excitation profile, and $\|\boldsymbol{G}(t)\|_2$ is the ℓ_2-norm of the gradient vector that scales the RF pulse according to k-space trajectory speed. The profile thicknesses can be calculated as follows:

$$\begin{aligned} \Delta z &= \frac{TBW_{SS}}{K_{SS}} \\ FOV_{PE} &= \frac{TBW_{PE}}{K_{PE}} \end{aligned} \tag{2.3}$$

Here, Δz and FOV_{PE} are the slice and slab thicknesses, respectively, and K_{SS} and K_{PE} are the covered k-space extents along the SS- and PE-axes, respectively. Additionally, TBW_{SS} and TBW_{PE} are time-bandwidth products (TBW) describing the slice and slab sharpnesses, respectively. The separation between the replicas along the SS-direction is:

$$\Delta d_{SS} = \frac{1}{\Delta k_{SS}} = \frac{N_{blip}}{K_{SS}} = \frac{N_{blip}}{TBW_{SS}} \Delta z \tag{2.4}$$

where Δk_{SS} is the distance between the consecutive trajectory lines, and N_{blip} is the number of blips in the SS gradient waveform. During a multislice acquisition, any overlap of the targeted slice with the replica profiles of other slices can cause a signal loss due to partial saturation [24]. The maximum number of slices, $N_{\max}$, that can be imaged while avoiding such a signal loss is defined as the number of slices that can fit between two consecutive replicas [23], i.e.,

$$N_{\max} = \frac{\Delta d_{SS}}{\Delta z} = \frac{N_{blip}}{TBW_{SS}}. \tag{2.5}$$

An increase in $N_{\max}$ can be achieved by either increasing N_{blip} or reducing TBW_{SS}, with the trade-offs of increased 2D RF pulse duration or reduced profile sharpness, respectively. Note that this definition of $N_{\max}$ assumes infinitely sharp slice profiles, i.e., ignores the relatively minor effect of the overlaps between the tails of consecutive slices [24].

As shown in Fig. 2.3c, the chemical shift of fat causes the fat profile to be displaced along the blipped SS-direction. This relative displacement, Δd, is expressed as follows:

$$\Delta d = \frac{T_{fast}\, \Delta f}{\Delta k_{SS}} = \frac{N_{blip}\, T_{fast}\, \Delta f}{TBW_{SS}} \Delta z = \frac{\Delta f}{BW_{SS}} \Delta z. \tag{2.6}$$

Here, T_{fast} is the duration of each trajectory line and BW_{SS} is the bandwidth along the SS-direction, such that $TBW_{SS} = N_{blip}\, T_{fast}\, BW_{SS}$. In addition, Δf is the resonance frequency difference between fat and water. Note that Δd can be quite prominent for 2D RF pulses due to low BW_{SS}. In fact, setting $BW_{SS} \leq \Delta f$ achieves a complete separation of fat and water profiles (i.e., $\Delta d \geq \Delta z$), enabling a subsequent 180° RF pulse to suppress the fat signal [23]. While the fat profile is also displaced along the PE-direction, the fast movement in k_{PE} causes this displacement to be negligibly small when compared to FOV_{PE}. In addition, the displacement in the PE-direction has no effect on fat suppression, since the 180° RF pulse is selective in the SS-direction only.

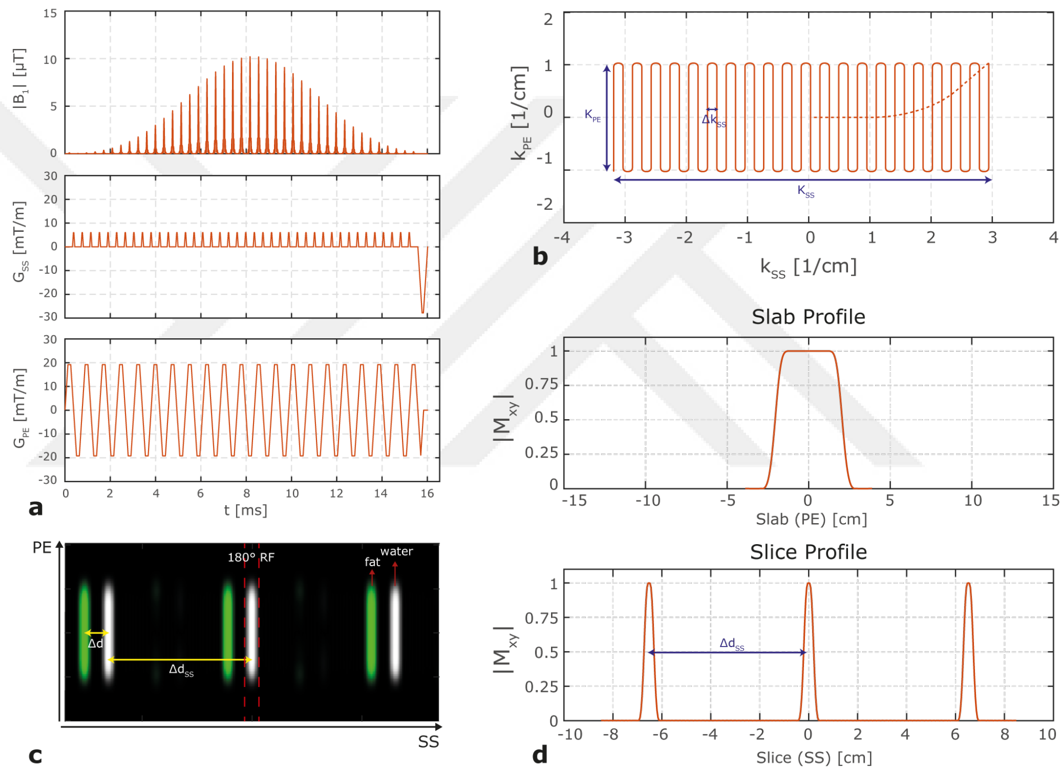

Figure 2.3: *The RF/gradient waveforms, k-space trajectory, and excitation profiles for a standard 2D RF pulse. (a) RF waveform, and gradient waveforms along the SS- and PE-directions (from top to bottom). (b) Excitation k-space trajectory for a standard 2D RF pulse, where K_{SS} and K_{PE} indicate the k-space coverage along the SS- and PE-directions, respectively. Δk_{SS} refers to the distance between two consecutive k-space lines. (c) The 2D excitation profile for the standard 2D RF pulse has replicas along the SS-axis, limiting the slice coverage to $N_{\max}$. Here, Δd indicates the distance between water and fat profiles, and Δd_{SS} indicates the separation between the replicas. (d) The slab and slice profiles of the standard 2D RF pulse. The design parameters were $FOV_{PE} = 40$ mm, $\Delta z = 4$ mm, $TBW_{SS} = 3$, $TBW_{PE} = 8$, and $N_{\max} = 16$.*

Under off-resonance effects such as B_0 field inhomogeneities or susceptibility differences, the 2D excitation profile experiences a shift along the blipped SS-direction, which can also be calculated using Eq. 2.6 with Δf corresponding to the off-resonance frequency this time. Since 2D RF pulses have long pulse durations, BW_{SS} is considerably smaller than that of a typical 180° RF pulse. Therefore, for a fixed Δf, the excitation profile of the 2D RF pulse experiences a considerably larger shift along the SS-direction when compared to that of the 180° RF pulse. The resulting mismatch between the excitation and refocusing profiles prevents complete refocusing of the excited slice, causing an effective loss of signal. This signal loss is position dependent due to the position dependence of Δf, causing an in-plane variability in the signal level. For fixed TBW_{SS}, longer 2D RF pulses have lower BW_{SS}, exhibiting increased off-resonance sensitivity. Note that while the 2D profile also shifts along the PE-direction, this shift is negligibly small and does not affect the mismatch with the refocusing profile, which acts along the SS-direction only.

Overall, Eqs. 2.5-2.6 show that robustness against off-resonance effects can be achieved only at the expense of reduced $N_{\max}$ or reduced T_{fast}, where the latter can only be achieved by reducing TBW_{PE}. Hence, standard 2D RF pulses exhibit a trade-off between off-resonance robustness vs. slice coverage and/or slab profile sharpness.

2.4 Tilted 2D Echo-Planar RF Pulse Design

The above-mentioned restrictions of the standard 2D RF pulses motivated alternative designs for 2D RF pulse excitations. A tilted 2D RF pulse design was developed to eliminate the slice coverage limitation of the standard 2D RF pulse [24]. This technique proposed rotating the excitation k-space trajectory such that the replicas are positioned outside the slice stack. The range of tilt angles θ that achieve unlimited slice coverage can be computed as follows [24]:

$$\theta \geq sin^{-1}\left(\frac{FOV_{PE}}{N_{\max}\,\Delta z}\right) = sin^{-1}\left(\frac{FOV_{PE}\,TBW_{SS}}{N_{blip}\,\Delta z}\right). \tag{2.7}$$

The echo-planar k-space trajectory is then tilted (i.e., rotated) by the minimum θ that satisfies Eq. 2.7. Since both N_{blip} and Δk_{SS} are kept fixed during rotation, the duration for the tilted 2D RF pulse is identical to that of the standard 2D RF pulse. Note that rotating the k-space trajectory causes a slight inefficiency in terms of k-space coverage. To compensate for this inefficiency, K_{PE} is slightly increased, so that the tilted trajectory traverses otherwise uncovered central frequencies. An example pair of standard and tilted 2D RF pulses are shown in Fig. 2.4.

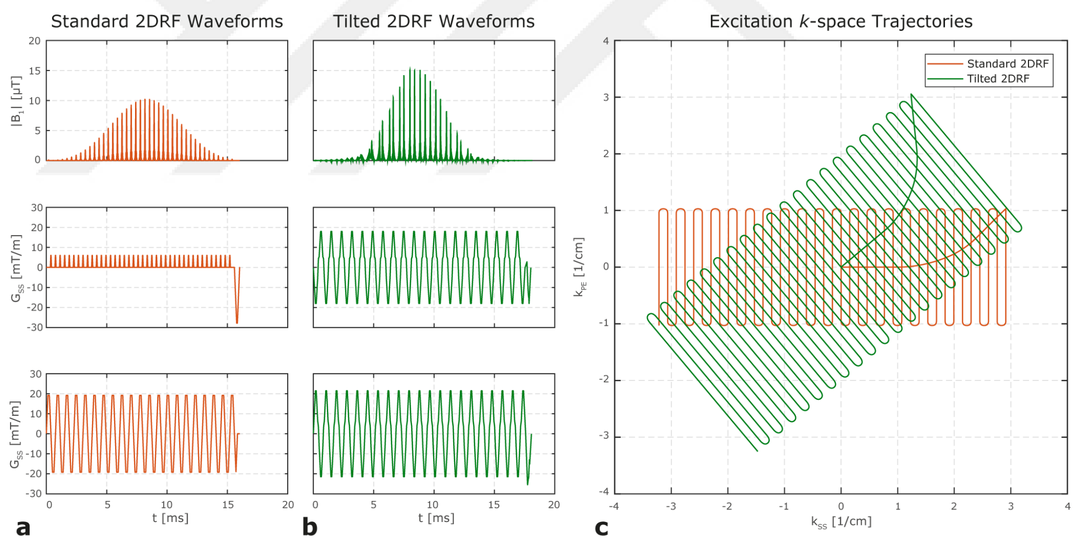

Figure 2.4: *The k-space trajectories and RF/gradient waveforms for a pair of standard and tilted 2D RF pulses. The RF and gradient waveforms for (a) the standard and (b) the tilted 2D RF pulses, with* 16.0 *ms and* 18.0 *ms pulse durations, respectively. (c) Excitation k-space trajectories for a standard 2D RF pulse and a tilted 2D RF pulse with* $\theta = 40°$. *For both pulses, VERSE was utilized to minimize pulse durations within the hardware limits. The design parameters were* $FOV_{PE} = 40$ *mm,* $\Delta z = 4$ *mm,* $TBW_{SS} = 3$*, and* $TBW_{PE} = 8$*. For the standard 2D RF pulse,* $N_{\max} = 16$.

Similar to the standard 2D RF pulse, the tilted 2D RF pulse provides a complete separation of water and fat profiles, allowing a subsequent 180° RF pulse to suppress the fat signal. However, the rotation results in poor coverage of the targeted k-space extent, causing degradation in 2D profiles [24]. Furthermore, the tilted 2D RF pulse does not achieve any reduction in pulse duration. Therefore, it provides minimal performance improvement over the standard 2D RF pulse in terms of through-plane off-resonance robustness.

Chapter 3

Sheared 2D RF Excitation

This chapter is based on the publication that is submitted to the Journal, Magnetic Resonance in Medicine and is titled "Barlas BA, Bahadir CD, Kafali SG, Yilmaz U, Saritas EU. Sheared 2D RF Excitation for Off-resonance Robustness and Fat Suppression in Reduced Field-of-View Imaging", submitted to Magnetic Resonance in Medicine, 2022.

3.1 Sheared 2D Echo-Planar RF Pulse Design

Using a small tip angle approximation, the excitation profile of a 2D RF pulse can be written as [44, 45]:

$$M(z,y) = C_2(\alpha)\, \mathcal{F}^{-1}\left\{W(k_{SS},k_{PE})S(k_{SS},k_{PE})\right\} \tag{3.1}$$

Here, z and y correspond to the SS- and PE-axes, respectively, $\mathcal{F}^{-1}$ denotes inverse Fourier transformation. $C_2(\alpha)$ contains all scaling parameters to set the flip angle α, and S is the unit sampling function induced by the excitation k-space trajectory. For a standard 2D RF pulse, covering k_{PE} axis continuously and k_{SS} axis discretely, S can be expressed as a summation of line impulses:

$$S(k_{SS}, k_{PE}) = \sum_{n=-\infty}^{\infty} \delta(k_{SS} - n\, \Delta k_{SS}). \tag{3.2}$$

Using Eq. 3.1, the excitation profile for a standard 2D RF pulse can then be derived as:

$$M(z, y) = \sum_{n=-\infty}^{\infty} w\left(\frac{z - n\, \Delta d_{SS}}{\Delta z}, \frac{y}{FOV_{PE}}\right) \tag{3.3}$$

where

$$w\left(\frac{z}{\Delta z}, \frac{y}{FOV_{PE}}\right) = \hat{C}_2(\alpha)\, \mathcal{F}^{-1}\left\{W(k_{SS}, k_{PE})\right\}. \tag{3.4}$$

Here, w denotes the desired 2D excitation profile (i.e., slice/slab thicknesses and sharpnesses) and $\hat{C}_2(\alpha) = C_2(\alpha)\, \Delta d_{SS}$ is a constant. Equation 3.3 confirms that the 2D excitation profile contains replicas along the SS-direction separated at Δd_{SS} distances, as previously given in Eq. 2.4.

The slice coverage limitation can be removed if the replicas are pushed outside the slice stack along the SS-direction. To achieve this, sheared trajectory is proposed to cover the excitation k-space, as shown in Fig. 3.1a. For shearing with angle θ applied to k_{SS} axis, the sheared version of S can be expressed as a summation of sheared line impulses, i.e.,

$$\begin{aligned} S_{shear}(k_{SS}, k_{PE}) &= \frac{1}{|cos(\theta)|}\, S(k_{SS} + k_{PE}\, tan(\theta), k_{PE}) \\ &= \frac{1}{|cos(\theta)|} \sum_{n=-\infty}^{\infty} \delta(k_{SS} + k_{PE}\, tan(\theta) - n\, \Delta k_{SS}) \end{aligned} \tag{3.5}$$

where the scaling by $|cos(\theta)|$ normalizes the sheared line impulses. Using Eq. 3.1, the excitation profile for the sheared 2D RF pulse can then be derived as:

$$M_{shear}(z,y) = \sum_{n=-\infty}^{\infty} w\left(\frac{z - n\,\Delta d_{SS}}{\Delta z}, \frac{y - n\,\Delta d_{SS}\,tan(\theta)}{FOV_{PE}}\right). \quad (3.6)$$

Accordingly, shearing does not change the profiles of the individual replicas, but only repositions them along the sheared axis, as displayed in Fig. 3.2b. These replicas are separated at Δd_{SS} and $\Delta d_{SS}\,tan(\theta)$ distances along the SS- and PE-directions, respectively, indicating that there is an angle θ between the sheared axis and the SS-axis. If the separation along the PE-direction is greater than FOV_{PE}, the replicas are completely pushed outside the slice stack, removing slice coverage limitations. The range of θ that satisfies this unlimited slice coverage criterion is:

$$\Delta d_{SS}\,tan(\theta) \geq FOV_{PE} \quad (3.7)$$

Using Eq. 2.4, this criterion can be re-written as:

$$\theta \geq tan^{-1}(FOV_{PE}\,\Delta k_{SS}) = tan^{-1}\left(\frac{FOV_{PE}\,TBW_{SS}}{N_{blip}\,\Delta z}\right). \quad (3.8)$$

For a desired 2D excitation profile, FOV_{PE}, TBW_{SS}, and Δz are all fixed. Hence, in theory, one can arbitrarily choose θ and compute the corresponding N_{blip} that guarantees unlimited slice coverage. According to Eq. 3.8, choosing a large θ allows using a small N_{blip}, such that the excitation k-space can then be covered in fewer lines, resulting in reduced pulse duration. Note that the displacement between the fat and the water profiles is also repositioned along the sheared axis, such that the displacement along the SS-direction is still equal to Δd as expressed in Eq. 2.6 and the displacement along the PE-direction is $\Delta d\ tan(\theta)$. For fixed TBW_{SS}, reduced pulse duration yields increased BW_{SS}, which in turn provides off-resonance robustness at the expense of potentially incomplete fat suppression. Therefore, θ should be chosen small enough to ensure successful fat suppression.

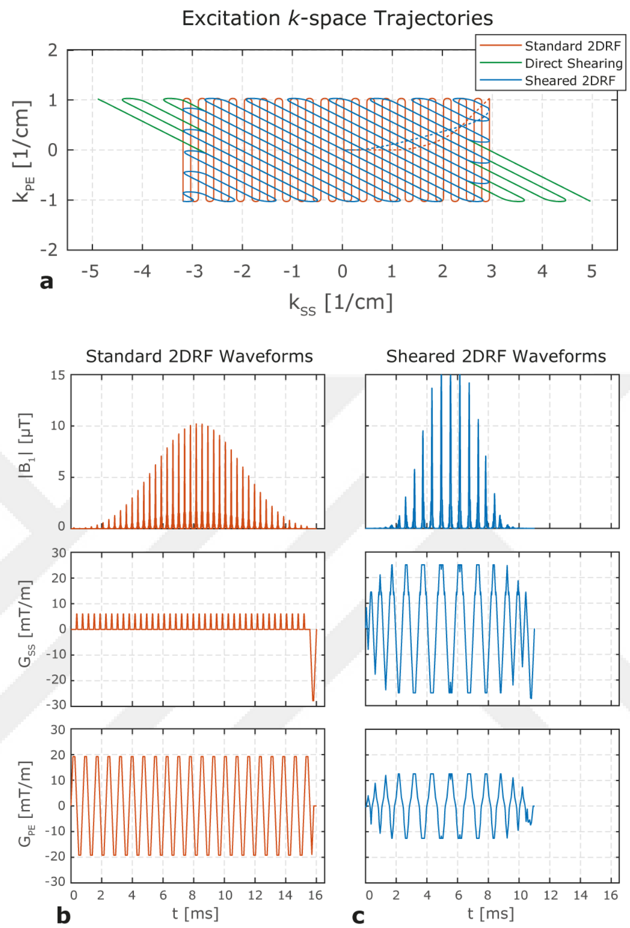

Figure 3.1: *The k-space trajectories and RF/gradient waveforms for standard and sheared 2D RF pulses. (a) Excitation k-space trajectories for a standard 2D RF pulse and a sheared 2D RF pulse with* $\theta = 63.25°$, *reducing* N_{blip} *from 40 to 14. Direct shearing (green) yields inefficient k-space coverage, whereas the proposed tailoring (blue) achieves identical k-space coverage as the standard 2D RF pulse. The dashed lines correspond to the rephasing gradient lobes during which the RF pulse is off. The RF and gradient waveforms for (b) the standard and (c) the sheared 2D RF pulses, with 16.0 ms and 11.0 ms pulse durations, respectively. The sheared design enables 31% reduction in pulse duration for this case. For both pulses, VERSE was utilized to minimize pulse durations within the hardware limits. The design parameters were* $FOV_{PE} = 40$ *mm,* $\Delta z = 4$ *mm,* $TBW_{SS} = 3$*, and* $TBW_{PE} = 8$*. For the standard 2D RF pulse,* $N_{\max} = 16$.

Figure 3.1 shows an example case for sheared 2D RF pulse design. For a given θ, first N_{blip} and Δk_{SS} are computed. Then, the sheared trajectory that gives the corresponding S_{shear} within the hardware limits is obtained. As seen in Fig. 3.1a, this "*direct shearing*" step yields an inefficient coverage of the excitation k-space: undesired coverage outside and missing coverage inside the targeted k-space extent will ultimately deteriorate the slice and slab profiles. Furthermore, the inefficiency of the coverage worsens with increasing θ. Therefore, tailoring the sheared trajectory is proposed to obtain identical coverage as the standard trajectory, as shown in Fig. 3.1a. In this tailored sheared trajectory, the corners of the targeted k-space extent are tucked in and filled by maintaining a fixed distance between the sheared trajectory lines. Note that the added lines do not alter the effective N_{blip} that determines the excitation profile, since $N_{blip} = K_{SS}/\Delta k_{SS}$ remains the same. Finally, the corresponding sheared 2D RF pulse can be computed using Eq. 2.2. As shown in Fig. 3.2, the replicas of the 2D excitation profile are along the SS-axis for the standard 2D RF pulses and along the sheared axis for the sheared 2D RF pulse. Likewise, the fat profiles demonstrate a large displacement from the water profile along the SS-axis for the standard 2D RF pulse and along the sheared axis for the sheared 2D RF pulse, enabling fat suppression using the 180° RF pulse of a spin echo sequence.

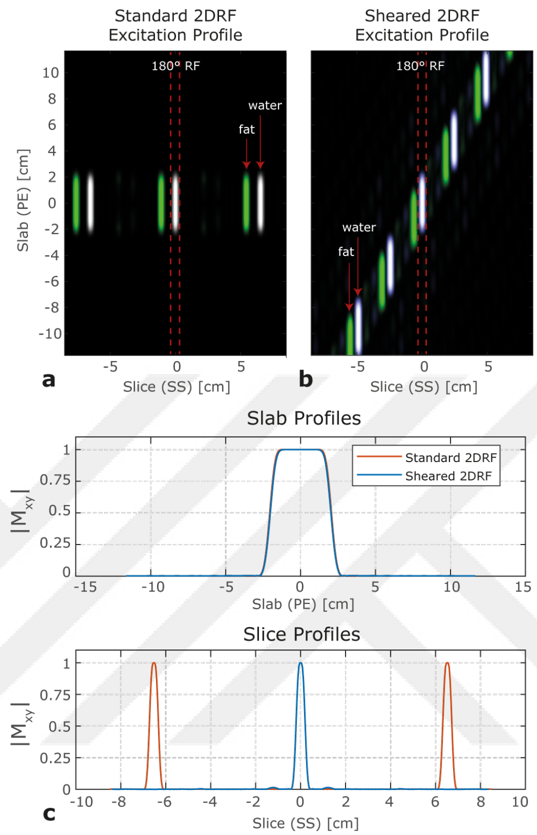

Figure 3.2: *The excitation profiles for standard and sheared 2D RF pulses. (a) The 2D excitation profile for the standard 2D RF pulse has replicas along the SS-axis, limiting the slice coverage to* $N_{\max} = 16$. *(b) The sheared 2D RF pulse with* $\theta = 63.25°$ *repositions the replicas along the sheared axis, removing slice coverage limitations. For both 2D RF pulses, both the displaced fat profiles and the replicas can be suppressed using a subsequent 180° refocusing RF pulse that is selective in SS-axis (dashed red lines). (c) 1D central cross-sections of water profiles along PE- and SS-axes demonstrate that the sheared design preserves profile sharpnesses along both axes. The design parameters were identical to those in Fig. 3.1.*

3.2 Methods

3.2.1 2D RF Pulse Design

MATLAB (MathWorks Inc., Natick, MA) was used for designing 2D RF pulses within the following hardware limits, based on the 3 T MRI scanner used in the experiments: $G_{\max} = 28$ mT/m maximum gradient amplitude and $S_{\max} = 150$ mT/m/ms maximum slew rate. Both RF and gradient waveforms were designed using 2 μs sampling time.

For a standard 2D RF pulse, first the gradient waveforms were designed directly within the hardware limits using the design parameters: $FOV_{PE} = 40$ mm, $\Delta z = 4$ mm, $TBW_{PE} = 8$, $TBW_{SS} = 3$, and $N_{\max} = 16$. Next, the RF waveform was designed assuming a constant gradient amplitude for the echo-planar k-space trajectory. Then, following Eq. 2.2, the RF waveform was scaled based on the time-varying gradient amplitudes using VERSE [46]. The resulting standard 2D RF pulse was slew-rate limited and did not benefit from further pulse duration minimization via VERSE [47].

For a sheared 2D RF pulse at a given θ, first N_{blip} and Δk_{SS} were computed according to Eq. 3.8. Then, the standard k-space trajectory was sheared using Eq. 3.5 and the separation distances were rescaled to Δk_{SS}. After tailoring this sheared trajectory to match the coverage of the standard trajectory, the corresponding gradient waveforms were computed. Next, the RF waveform on the standard trajectory was interpolated to the sheared trajectory using scattered interpolation. Note that the shearing and separation adjustment operations can cause the hardware limits to be exceeded. Thus, VERSE was utilized to compute the minimum duration RF/gradient waveforms within the hardware limits with peak $B_1 = 15$ μT [47]. Figure 3.3 shows an example case before and after this VERSE step, where the pulse duration increases from 7.3 ms to 11.0 ms to enforce the hardware limits.

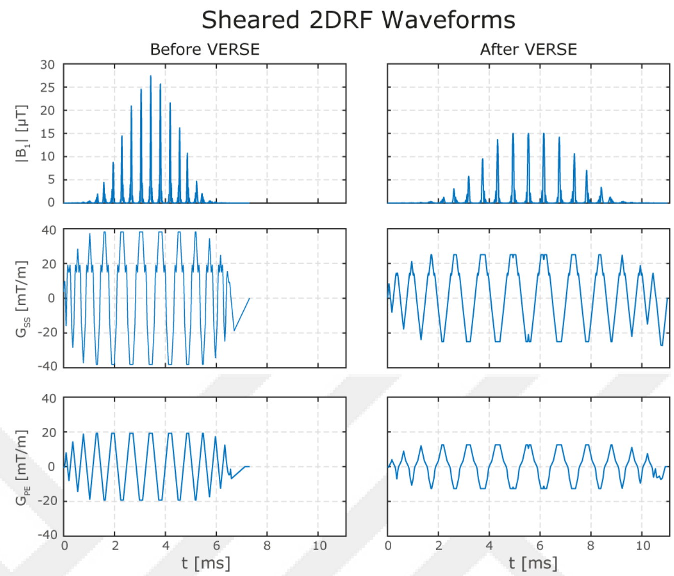

Figure 3.3: *The sheared 2D RF pulse from Fig. 3.1, before and after applying VERSE to generate the minimum duration pulse within the hardware limits ($G_{\max} = 28$ mT/m, $S_{\max} = 150$ mT/m/ms, peak $B_1 = 15$ μT). The pulse before VERSE significantly exceeds the hardware limits, as it was computed by shearing the k-space trajectory without any constraints. After applying VERSE, the pulse duration increases from 7.3 ms to 11.0 ms. This sheared 2D RF pulse is 31% shorter than its standard counterpart, which has 16.0 ms duration.*

3.2.2 Simulations

Simulations were performed in MATLAB to evaluate the performances of the 2D RF pulses. Fat profiles were simulated for $\Delta f = 440$ Hz at 3 T. For all simulations, T_1/T_2 relaxation effects were ignored when simulating the excitation profiles.

First, the duration and fat suppression capability of the sheared 2D RF design were evaluated as a function of θ. Based on the designed standard 2D RF pulse, sheared 2D RF pulses with θ ranging between 30° to 80° were generated, using the minimum N_{blip} that satisfies the unlimited slice coverage criterion in Eq. 3.8 at each θ. Next, the ratio of the total fat signal and water signal in the 2D excitation profile after applying a 180° RF pulse was used as the performance metric for fat suppression. Here, the target fat/water signal ratio as 5%, i.e., corresponding to a goal of 95% fat suppression, is set. To compute their respective signals, the refocused fat and water profiles were integrated along the SS-axis (by incorporating through slice phase variations) at $PE = 0$ mm. The 180° refocusing pulse was exported from the stock ssEPI sequence used in the MRI experiments, and was a standard three-lobe sinc-shaped RF pulse with 2.34 ms duration and $BW_{SS} = 1709$ Hz.

Next, to analyze the effects of the design parameters on the sheared 2D RF pulse duration, each design parameter was varied while keeping other parameters fixed based on the parameters of the 16 ms standard 2D RF pulse given above. FOV_{PE} was varied between 30-60 mm, TBW_{PE} was varied between 6-10, Δz was varied between 3-5 mm, and TBW_{SS} was varied between 2-4. Furthermore, to investigate the effects of hardware limits, $G_{\max}$ was varied between 20-40 mT/m and $S_{\max}$ was varied between 100-200 mT/m/ms. For each parameter set, a standard 2D RF pulse and sheared 2D RF pulses with θ ranging between 30° to 80° were generated to demonstrate the trade-offs in sheared 2D RF design.

Finally, to quantitatively compare the off-resonance robustness performances of the standard and sheared 2D RF pulses, Bloch simulations were performed for off-resonance frequencies ranging between $\Delta f = \pm 160$ Hz, i.e., corresponding to ± 1.25 ppm at 3 T. For each case, the center of mass for the main lobe of the 2D excitation profile before and after the 180° RF pulse was computed to quantify the off-resonance induced displacements. In addition, the in-plane signal level after the 180° RF pulse was evaluated as a function of off-resonance frequency and PE-position. At a given off-resonance frequency, the in-plane signal was computed by integrating the refocused 2D profile along the SS-axis, followed by a normalization with respect to the in-plane signal for $\Delta f = 0$ Hz and $PE = 0$ mm. To quantify the improvement in off-resonance robustness achieved by the sheared 2D RF design, the signal ratios between sheared and standard 2D profiles were calculated as a function of off-resonance frequency and PE-position.

3.2.3 MRI Experiments

In vivo and phantom imaging experiments were conducted on a 3 T MRI scanner (Siemens Magnetom Trio) using an 8-channel spine array coil. In vivo imaging was conducted under the approval of the institutional review board. The stock ssEPI sequence was programmed in the IDEA pulse sequence programming environment to allow interchanging the excitation pulse between the following two options: (1) a standard 1D RF pulse preceded by an additional frequency-selective fat suppression RF pulse, or (2) a 2D RF pulse without any additional fat suppression. For these experiments, the standard and sheared 2D RF pulses featured in Fig. 3.1 were utilized, where the standard 2D RF pulse had 16.0 ms duration and sheared 2D RF pulse had 11.0 ms duration for $\theta = 63.25°$. For both 2D RF pulses, the minimum dwell times of the MRI scanner were utilized, which were 2 μs for RF waveforms and 10 μs for gradient waveforms. The gradient waveforms were downsampled accordingly.

The phantom experiments were performed on a custom-built 1:1 scale head and neck phantom reflecting the anatomy of the brain and cervical spine [48]. In vivo experiments were conducted with three human subjects (2 females, 1 male). For both the phantom and in vivo imaging experiments, the entire cervical spine region was covered via multislice T2-weighted ssEPI images acquired in the sagittal plane. For reduced-FOV imaging using the standard and sheared 2D RF pulses, the imaging parameters were: 200×50 mm^2 FOV, 128×32 acquisition matrix. The echo time was $TE = 27$ ms and $TE = 22$ ms for the standard and sheared 2D RF pulse cases, respectively. Here, the 5 ms reduction in pulse duration allowed 5 ms reduction in TE for the sheared 2D RF pulse case. For full-FOV imaging using the 1D RF pulse with additional fat suppression, the imaging parameters were: 200×162.5 mm^2 FOV, 128×104 acquisition matrix, and $TE = 50$ ms. Other imaging parameters were kept fixed between the reduced-FOV and full-FOV cases: 1.6×1.6 mm^2 in-plane resolution, $\Delta z = 4$ mm, 7 slices, $BW = 1860$ Hz/Px, $TR = 6500$ ms, $N_{ave} = 32$ (number of averages), and 6/8 partial Fourier acquisition.

Next, to quantitatively evaluate the off-resonance robustness of the 2D RF pulses, off-resonance field maps were acquired using a double-echo gradient echo (GRE) sequence with the following parameters: $TE1 = 5.19$ ms, $TE2 = 7.65$ ms, 1.2×1.2 mm^2 in-plane resolution, $\Delta z = 4$ mm, 7 slices, 300×300 mm^2 FOV, 256×256 acquisition matrix. The phase maps from the GRE sequence were phase unwrapped, and the off-resonance frequency maps were computed using the following relation:

$$\Delta f = \frac{\Delta \phi}{2\pi \Delta TE} \tag{3.9}$$

Here, $\Delta\phi$ is the unwrapped phase and $\Delta TE = 2.46$ ms is the difference between $TE1$ and $TE2$. Since this ΔTE corresponds to 2π phase difference for $\Delta f =$ 440 Hz, the resulting off-resonance map excluded the effects of chemical shift of fat. Note that the off-resonance map and ssEPI images do not align anatomically, since off-resonance causes a position-dependent shift (i.e., distortion) along the PE-direction in ssEPI images (see Eq. 2.1) [42]. After compensating for this shift, Δf at all pixels in the ssEPI images were determined using the off-resonance map. Next, pixel-wise signal ratios for the reduced-FOV images from the standard and sheared 2D RF cases were computed and plotted as a function of Δf at the corresponding pixels. These signal ratios were then compared with the theoretical signal ratios from simulations by taking into account the 5 ms difference in TE for the standard vs. sheared 2D RF pulse cases. Here, the reduced TE further improves the signal ratio in favor of the sheared 2D RF pulse as follows: The agar-agar gel in the custom-built phantom was previously measured to have $T_2 =$ 61.9 ms [48], corresponding to 1.084 fold improvement in signal ratio for 5 ms reduction in TE. Likewise, for the in vivo experiments, $T_2 = 73$ ms for white matter of the spinal cord [49] yields 1.071 fold improvement in signal ratio. Lastly, the theoretical signal ratios were multiplied by these additional improvements and compared with the pixel-wise signal ratios from the experiments.

3.3 Results

An example case comparing standard and sheared 2D RF pulses is demonstrated in Fig. 3.1. Here, the standard 2D RF pulse has $N_{blip} = 40$, while the sheared 2D RF pulse has $\theta = 63.25°$ with $N_{blip} = 14$. The corresponding RF and gradient waveforms are displayed in Fig. 3.1b-c, where the resulting durations are 16.0 ms and 11.0 ms for the standard and sheared 2D RF pulses, respectively, providing 31.25% shortening of the pulse duration with the sheared design. Next, the corresponding 2D excitation profiles and 1D profiles along the PE- and SS-axes are shown in Fig. 3.2, validating the fidelity of the slice and slab profiles for the sheared 2D RF design. For both 2D RF pulses, $FOV_{PE} = 40$ mm, $\Delta z = 4$ mm, $TBW_{SS} = 3$, and $TBW_{PE} = 8$. For the standard 2D RF pulse, the replicas are located along the SS-axis, limiting the slice coverage to $N_{\max} = 16$. In contrast, the sheared 2D RF design positions the replicas along the sheared axis, providing unlimited slice coverage. In both cases, the fat profiles demonstrate a relative displacement with respect to the water profile, enabling fat suppression using a subsequent 180° RF pulse.

Figure 3.4 shows the duration and fat suppression capability of the sheared 2D RF pulse design as a function of θ for the same design parameters as in Fig. 3.1. For a standard 2D RF pulse with 16 ms duration, Fig. 3.4a shows 1D cross-sections along the SS-axis for water and fat profiles before and after the 180° RF pulse, in the absence of other off-resonance effects. As seen in this figure, the signal from fat is completely suppressed after the 180° RF pulse, yielding a fat/water signal ratio $< 0.02\%$. Figure 3.4b shows water and fat profiles for a sheared 2D RF pulse with $\theta = 63.25°$ and 11.0 ms pulse duration. For fixed TBW_{SS}, the reduced pulse duration causes an increase in BW_{SS}, resulting in a slight overlap of fat profiles for the sheared 2D RF pulse and the 180° RF pulse. For this case, the fat/water signal ratio was computed as 5%. This analysis was repeated for θ ranging between 30° to 80°. As seen in Fig. 3.4c, the sheared 2D RF pulse duration decreases steadily as a function of θ, with $\theta > 42°$ yielding pulses shorter than the standard 2D RF pulse. On the other hand, Fig. 3.4d shows that the fat/water signal ratio remains relatively low for small θ, but increases rapidly for $\theta > 65°$. When evaluated together, the results in Fig. 3.4c-d clearly display the trade-offs in the sheared design: a small θ causes the pulse duration to increase as it requires large N_{blip} to satisfy the unlimited slice coverage criterion (see Eq. 3.8), whereas a large θ jeopardizes the fat suppression capability due to increased BW_{SS}. Setting a target fat/water signal ratio of 5% enables us to choose an optimal θ. Accordingly, for the given set of design parameters, the shortest sheared 2D RF pulse that satisfies the 5% target has optimal $\theta = 63.25°$ with 11.0 ms duration (i.e., the case featured in Fig. 3.4b).

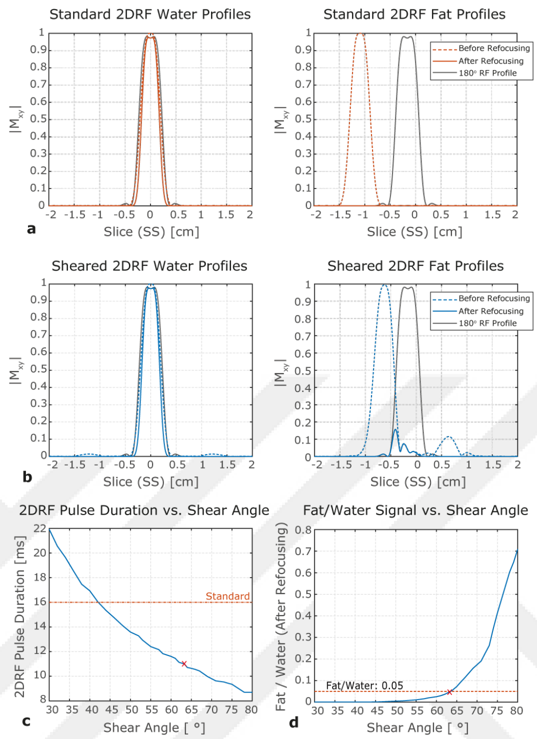

Figure 3.4: *The durations and fat suppression capabilities of standard and sheared 2D RF pulses as a function of θ. 1D cross-sections of water and fat profiles along the SS-axis for (a) the standard 2D RF pulse and (b) the sheared 2D RF pulse with $\theta = 63.25°$ (i.e., the pulses in Fig. 3.1), before and after the $180°$ refocusing RF pulse. Water and fat profiles for the $180°$ RF pulse are also shown (gray lines). While the signal from fat is completely suppressed for the standard design, a residual fat signal corresponding to an effective fat/water signal ratio of 5% is refocused for the sheared design. (c) The pulse duration and (d) the fat/water signal ratio for the sheared 2D RF pulse as a function of θ ranging between $30°$ to $80°$. The shortest sheared 2D RF pulse that provides a target fat/water ratio of 5% has optimal $\theta = 63.25°$ with 11.0 ms duration (red crosses). The design parameters were identical to those in Fig. 3.1.*

The effects of design parameters and hardware limits on the sheared 2D RF pulse duration are shown in Fig. 3.5, together with the corresponding standard 2D RF pulse durations. According to Fig. 3.5a, while decreasing FOV_{PE} increases the standard 2D RF pulse duration, it decreases the sheared 2D RF pulse duration. The former result is consistent with Eq. 2.3, where smaller FOV_{PE} requires an increase in K_{PE} for fixed TBW_{PE}, which in turn extends the k-space coverage and increases the pulse duration. In contrast, for the sheared 2D RF pulse, Eq. 3.8 shows that smaller FOV_{PE} results in reduced N_{blip} for a fixed θ. This effect outweighs the former one and results in reduced pulse duration for the sheared 2D RF pulse. For both standard and sheared 2D RF pulses, the pulse duration increases with increasing TBW_{PE}. This result is consistent with Eq. 2.3, since an increase in TBW_{PE} requires an increase K_{PE}. Figure 3.5b shows that while Δz has a negligible effect on the standard 2D RF pulse duration, the sheared 2D RF pulse duration increases with decreasing Δz. While Eq. 2.3 shows that a decrease in Δz requires an increase in K_{SS}, this can easily be achieved for the standard 2D RF pulse by increasing the area under each gradient blip, without changing N_{blip} or the pulse duration. In contrast, for the sheared 2D RF pulse, Eq. 3.8 shows that a decrease in Δz requires an increase in N_{blip} for a fixed θ, which in turn increases the pulse duration. For both standard and sheared 2D RF pulses, the pulse duration increases with increasing TBW_{SS}. This can be confirmed using Eq. 2.5 for the standard 2D RF pulse, where an increase in TBW_{SS} requires an increase in N_{blip} for fixed $N_{\max}$. Likewise, for the sheared 2D RF pulse, Eq. 3.8 shows that larger TBW_{SS} requires a larger N_{blip} for a fixed θ. As shown in Fig. 3.5c, $G_{\max}$ has a minimal effect on both the standard and sheared 2D RF durations, apart from a slight increase in sheared 2D RF pulse duration at low $G_{\max}$. In contrast, decreasing $S_{\max}$ increases both the standard and sheared 2D RF durations. Note that these results are consistent with Fig. 3.1b-c, where the gradient waveforms are dominated by the slew rate limits. Overall, these results demonstrate that the shearing operation generates 2D RF pulses with considerably reduced durations for a wide range of θ. For the parameters considered here, the optimal θ that satisfies the target fat/water signal ratio of 5% varies between 54°-74° (marked with red crosses in Fig. 3.5). Note that for the cases where $TBW_{SS} = 3$ was kept fixed (i.e., all results in Fig. 3.5 except for the analysis on TBW_{SS}), the optimal θ corresponds to pulse durations around 11 ms. For larger TBW_{SS}, the optimal θ is reached at longer pulse durations. These results are consistent with Eq. 2.6, where targeting specific fat profile displacement (analogous to targeting a specific fat/water signal ratio) is equivalent to fixing BW_{SS}.

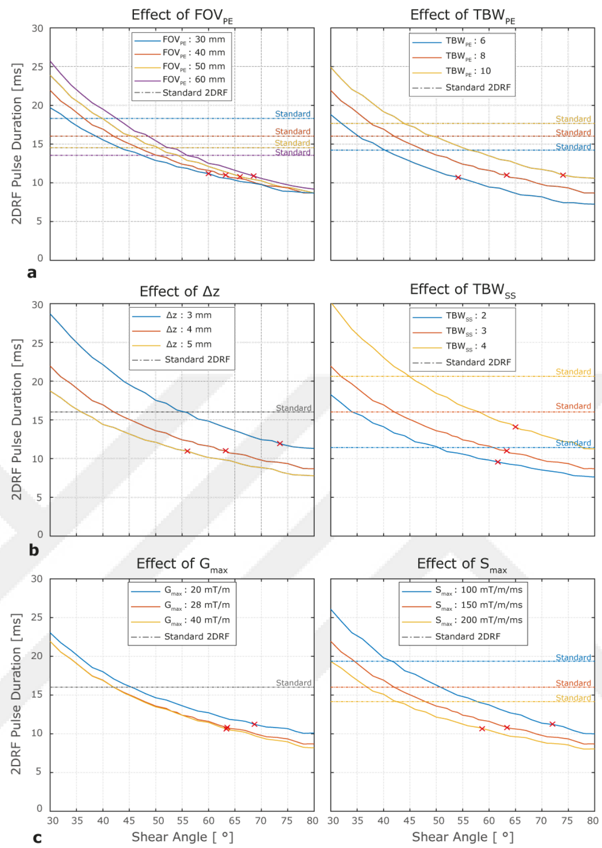

Figure 3.5: *The effects of the design parameters and hardware limits on the pulse duration as a function of θ. (a) A decrease in FOV_{PE} increases the standard 2D RF pulse duration (dashed lines), while it decreases the sheared 2D RF pulse duration. Increasing TBW_{PE} increases both the standard and sheared 2D RF pulse durations. (b) The standard 2D RF pulse duration is unaffected from Δz (as shown in gray dashed line for all Δz), whereas the sheared 2D RF pulse duration increases with decreasing Δz. An increase in TBW_{SS} increases both the standard and sheared 2D RF pulse durations. (c) Pulse durations are minimally affected by $G_{\max}$ but increase with decreasing $S_{\max}$ for both the standard and sheared 2D RF pulses. Overall, the sheared design generates pulses with considerably reduced durations. The red crosses indicate the sheared 2D RF pulses with optimal θ that satisfies the target fat/water signal ratio of 5%. Each parameter was varied while keeping others fixed, with default values of $FOV_{PE} = 40$ mm, $TBW_{PE} = 8$, $\Delta z = 4$ mm, $TBW_{SS} = 3$, $G_{\max} = 28$ mT/m, and $S_{\max} = 150$ mT/m/ms. For the standard 2D RF pulse, $N_{\max} = 16$.*

Off-resonance robustnesses of the standard and sheared 2D RF pulses are compared in Fig. 3.6. In Fig. 3.6a-b, the 2D profiles of the standard and sheared 2D RF pulses before and after the 180° refocusing RF pulse are displayed for on-resonance and $\Delta f = 64$ Hz off-resonance cases. As expected, the 2D standard and sheared profiles are almost identical for the on-resonance case, both before and after refocusing. In contrast, for $\Delta f = 64$ Hz case, the 2D profiles before refocusing demonstrate that the sheared 2D profile experiences a visibly reduced shift along the SS-direction due to its shorter pulse duration (i.e., larger BW_{SS}) when compared to the standard 2D profile. Comparing the 2D profiles after refocusing at $\Delta f = 64$ Hz, the effective slice for the sheared 2D profile exhibits only a minimal signal loss due to partial refocusing effects and is visibly thicker than the standard 2D profile. Next, Fig. 3.6c demonstrates the off-resonance induced displacements in the center of mass for the main lobe of the 2D profiles before and after refocusing, for off-resonance frequency ranging between $\Delta f = \pm 160$ Hz. While the displacement for the standard 2D profile is mainly along the SS-direction with a negligibly small shift along the PE-direction, the sheared 2D profile displaces along both the SS- and PE-directions (i.e., along the sheared axis), as expected. Note that the displacement of the sheared 2D profile along the PE-direction is relatively small when compared to FOV_{PE}, and would therefore not induce a major problem during imaging. In contrast, the reduction in the displacement along the SS-direction is significant when compared to Δz, highlighting the off-resonance robustness achieved by the sheared 2D RF design.

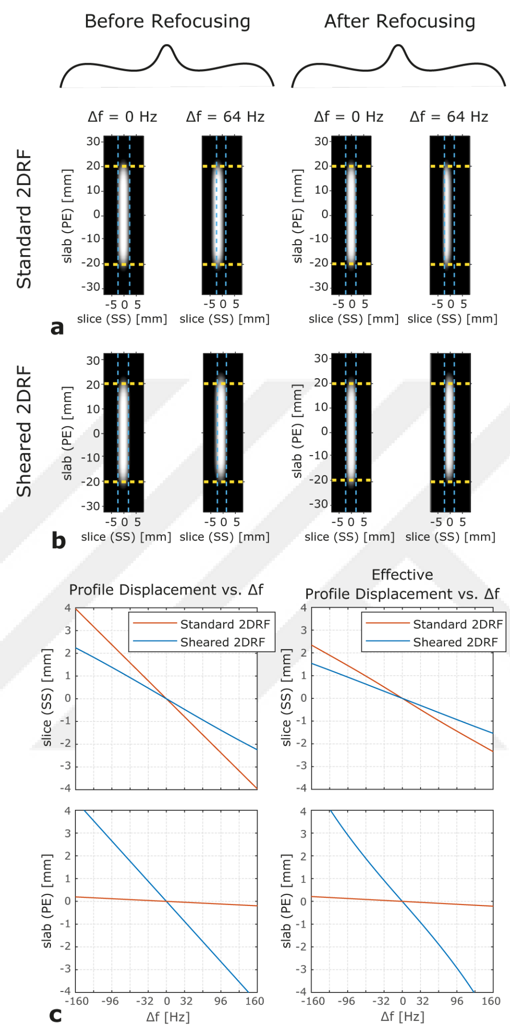

Figure 3.6: *The comparison of off-resonance robustnesses for the standard and sheared 2D RF pulses. The 2D profiles of (a) the standard and (b) the sheared 2D RF pulses before and after a* 180° *RF pulse for on-resonance and* $\Delta f = 64$ *Hz off-resonance cases. For reference, the borders of the targeted slab and slice thicknesses* ($FOV_{PE} = 40$ *mm and* $\Delta z = 4$ *mm) are marked with yellow and blue lines, respectively. The 2D profiles after refocusing are almost identical for the on-resonance case, whereas the effective slice for the sheared 2D RF pulse is visibly thicker for 64 Hz off-resonance case. (c) The profile displacements along the PE- and SS-directions before and after refocusing under off-resonance ranging between* $\Delta f = \pm 160$ *Hz. The displacement is mainly along the SS-axis for the standard 2D RF pulse and along the sheared axis for the sheared 2D RF pulse. The displacement along the SS-direction is significantly reduced for the sheared 2D RF profile, highlighting its through-plane off-resonance robustness. The design parameters were identical to those in Fig. 3.1.*

Next, Fig. 3.7 compares the in-plane signal levels for the standard and sheared 2D RF pulses as a function of off-resonance frequency and PE-position. These comparisons ignore relaxation effects to highlight the differences stemming from the excitation profiles alone. The signal level for the standard 2D RF pulse rapidly decreases with increasing off-resonance frequency, whereas the sheared 2D RF pulse maintains a high signal level for a wide range of off-resonance frequencies. For example, at $\Delta f = \pm 128$ Hz and $PE = 0$ mm, the signal levels are 0.82 and 0.48 for the sheared and standard 2D RF pulses, respectively, yielding a signal ratio of 1.71 (i.e., 71% improvement in signal). However, for the sheared 2D profile, the displacement along the PE-direction shown in Fig. 3.6c causes an asymmetry in signal level as a function of PE-position. The signal ratio between the sheared and standard 2D profiles as a function of off-resonance frequency and PE-position is shown in Fig. 3.7c. In the central $0.6FOV_{PE}$ region around the slab center, the sheared 2D RF pulse achieves increasing levels of signal ratio under increasing Δf. For off-central PE-positions, the signal ratio further increases in the proximity of the sheared axis. For PE-positions distant to the sheared axis, the signal level of the sheared 2D RF pulse is lower than its standard counterpart. Figure 3.7d provides a summary result for this position-dependent nature of the signal ratio, showing the median and $25^{th} - 75^{th}$ percentiles for the signal ratio across the PE-direction as a function of Δf. Note that the distribution around the median is quite narrow and closely matches the signal ratio at $PE = 0$ mm, indicating that the aforementioned displacement of the sheared 2D profile along the PE-direction has a minor effect on the signal ratio. Importantly, the signal ratio exceeds 2 (i.e., 100% improvement in signal) for $|\Delta f| > 146$ Hz, highlighting the off-resonance robustness achieved by the sheared 2D RF design.

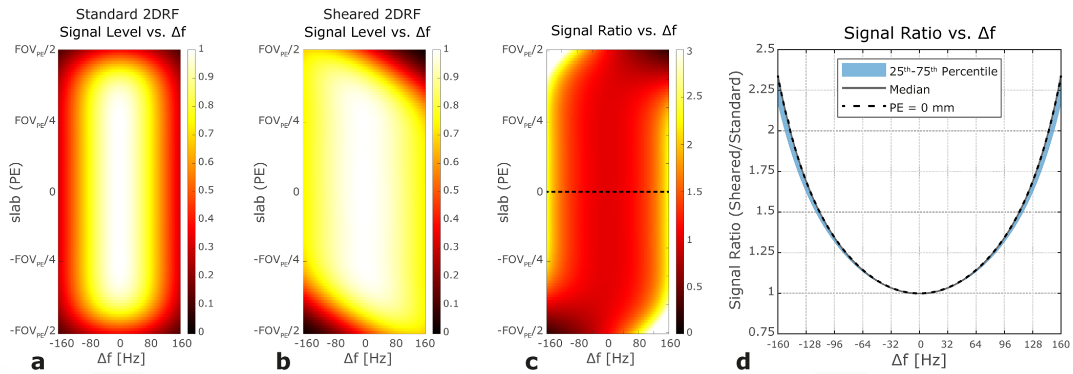

Figure 3.7: *The in-plane signal levels for the standard and the sheared 2D RF profiles as a function of off-resonance frequency and PE-position. (a) For the standard case, the signal level is rapidly decreasing with increasing off-resonance. (b) The signal level for the sheared 2D RF pulse is preserved for a wide range of* Δf*, with an asymmetry along the PE-direction due to the profile displacement along the sheared axis. (c) The signal ratio between the sheared and standard 2D RF pulses as a function of off-resonance and PE-position. In the central* $0.6FOV_{PE}$ *region, the sheared 2D RF pulse achieves increasing levels of signal ratio for increasing* Δf*. Off-central PE-positions demonstrate even higher signal ratio in the proximity of the sheared axis. (d) The signal ratio (median and* 25^{th}*-*75^{th} *percentiles) across the PE-direction as a function of* Δf*. The distribution closely follows the signal ratio at* $PE = 0$ *mm (black dashed line). The design parameters were identical to those in Fig. 3.1. These simulations ignored* T_1/T_2 *relaxation effects.*

Figure 3.8 shows the phantom imaging results for the central slice of the sagittal slice stack. The GRE image in Fig. 3.8a marks the graphical prescription of the full FOV and reduced FOV, and Fig. 3.8e shows the off-resonance map from the double-echo GRE sequence. As seen in Fig. 3.8b, off-resonance effects cause severe in-plane distortions in the full-FOV image acquired using a 1D RF pulse. In contrast, both of the reduced-FOV images in Fig. 3.8c-d successfully alleviate these distortions and yield ssEPI images that depict the anatomy of the phantom more accurately. Furthermore, the sheared 2D RF pulse accomplishes substantial signal improvement in regions that exhibit high off-resonance, such as the upper cervical spine region (red arrows). Figure 3.8f compares the scatter plot of the experimental signal ratio with the theoretical signal ratio (with and without 5 ms TE difference taken into account), showing a close match between the two especially for the case where the TE difference is included. Here, the experimental signal ratio was computed for the reduced-FOV images from the sheared and standard 2D RF designs, and Δf for each pixel was determined using the off-resonance map after taking into account the distortion in PE-direction for ssEPI images (see Eq. 2.1). To avoid background and signal pileup regions, only the pixels with intensities within 25%-67% of the maximum pixel intensity were utilized. Overall, the experimental results demonstrate a slightly higher signal ratio than expected theoretically. Importantly, the signal ratio is smaller than 1 for only 0.5% of pixels. In contrast, it exceeds 1.25 for 46.8% and 1.5 for 11.7% of pixels across the entire reduced FOV.

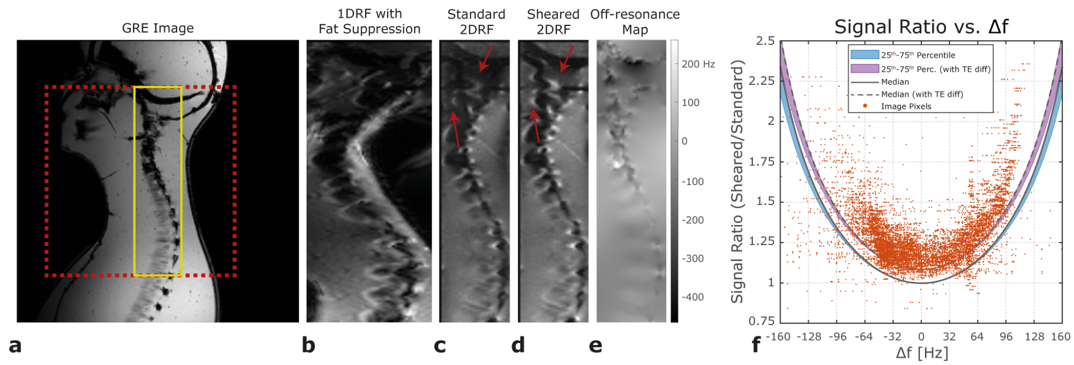

Figure 3.8: *Phantom imaging results from the spine region of a custom-built head and neck phantom. (a) One of the GRE images from the double-echo GRE sequence, with the prescribed full-FOV (red dashed rectangle) and reduced-FOV (yellow rectangle) regions marked for reference. (b) The full-FOV image (cropped version shown), which was acquired using a 1D RF pulse with additional frequency-selective fat suppression, suffers from severe in-plane distortions. The reduced-FOV images that were acquired using (c) the standard and (d) the sheared 2D RF pulses accomplish high-resolution images with reduced in-plane distortions. The sheared 2D RF pulse substantially improves the signal levels, especially in regions exposed to high off-resonance (red arrows). (e) The off-resonance map obtained from the double-echo GRE sequence. (f) The experimental signal ratios (computed for the reduced-FOV images from the sheared and standard 2D RF pulses) are plotted together with the theoretical signal ratios (with and without the TE difference taken into account), showing a close match especially for the case where the TE difference is included. These results demonstrate that the sheared 2D RF pulse improves the signal level in the presence of off-resonance effects.*

Finally, Fig. 3.9a-e shows in vivo imaging results for Subject 1, covering the entire cervical spine sagittally. Again, both reduced-FOV images alleviate in-plane distortions when compared to the full-FOV image. Furthermore, the sheared 2D RF design significantly improves the signal level in regions experiencing high off-resonance (see Fig. 3.9e for off-resonance map), especially in the central cervical spine and upper thoracic spine regions (red arrows). Detailed in vivo imaging results for Subject 2 and Subject 3 are provided in Fig. 3.10b-c. For these two subjects, fat suppression during full-FOV imaging failed in lower cervical spine region, causing the displaced fat signal to overlap with and obscure the spinal cord (yellow arrows). In contrast, both the standard and sheared 2D RF pulses demonstrate high fidelity fat suppression in addition to reduced in-plane distortions. Furthermore, the sheared 2D RF design shows higher signal levels in regions of high off-resonance. Figure 3.9f shows the signal ratio between the reduced-FOV in vivo images for all three subjects, in comparison to the theoretical signal ratio (with and without 5 ms TE difference taken into account). Here, the signal ratio was computed for pixels within ROIs manually drawn on the spinal cord region of each subject as shown in Fig. 3.10. The in vivo results confirm the signal improvement achieved by the off-resonance robustness of the sheared 2D RF design. Similar to the case in the phantom imaging results, in vivo results exhibit a slightly higher signal ratio than expected. Across all subjects, the signal ratio is smaller than 1 for only 2.2% of pixels within ROIs. In contrast, it exceeds 1.25 for 53.2% and 1.5 for 21.3% of pixels within ROIs. These results emphasize that a large percentage of pixels within the spinal cord significantly benefit from the sheared 2D RF design, due to the abundance of off-resonance effects around the spine.

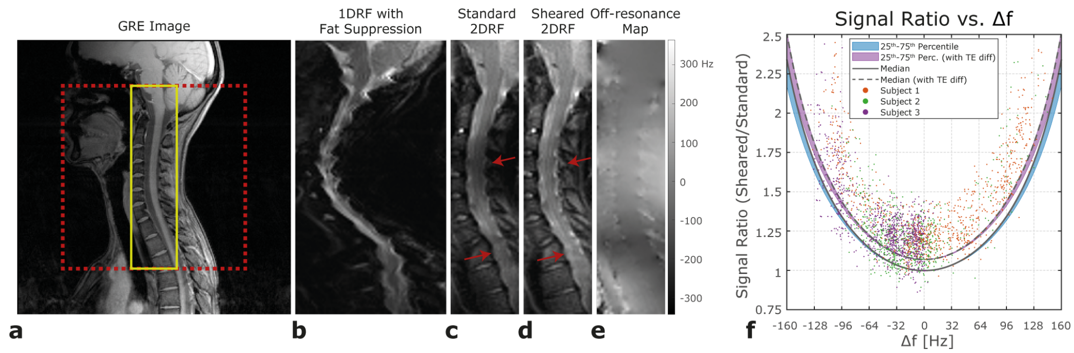

Figure 3.9: *In vivo imaging results in the sagittal plane from the cervical spine of Subject 1 and signal ratio analysis for all three subjects. (a) One of the images from the double-echo GRE sequence, showing the anatomy together with the full-FOV (red dashed rectangle), and reduced-FOV (yellow rectangle) regions marked for reference. (b) The full-FOV image (cropped version shown) suffers from severe in-plane off-resonance distortions. The reduced-FOV images with (c) the standard and (d) the sheared 2D RF pulses alleviate these distortions and achieve high-resolution images. The sheared 2D RF pulse accomplishes remarkable signal improvement in regions exposed to high off-resonance (red arrows). (e) The off-resonance map from the double-echo GRE sequence. (f) The experimental signal ratios between the sheared and standard reduced-FOV images for all three subjects show a close agreement with the theoretical signal ratios (plotted with and without the TE difference taken into account), confirming the signal improvement achieved via the off-resonance robustness of the sheared design.*

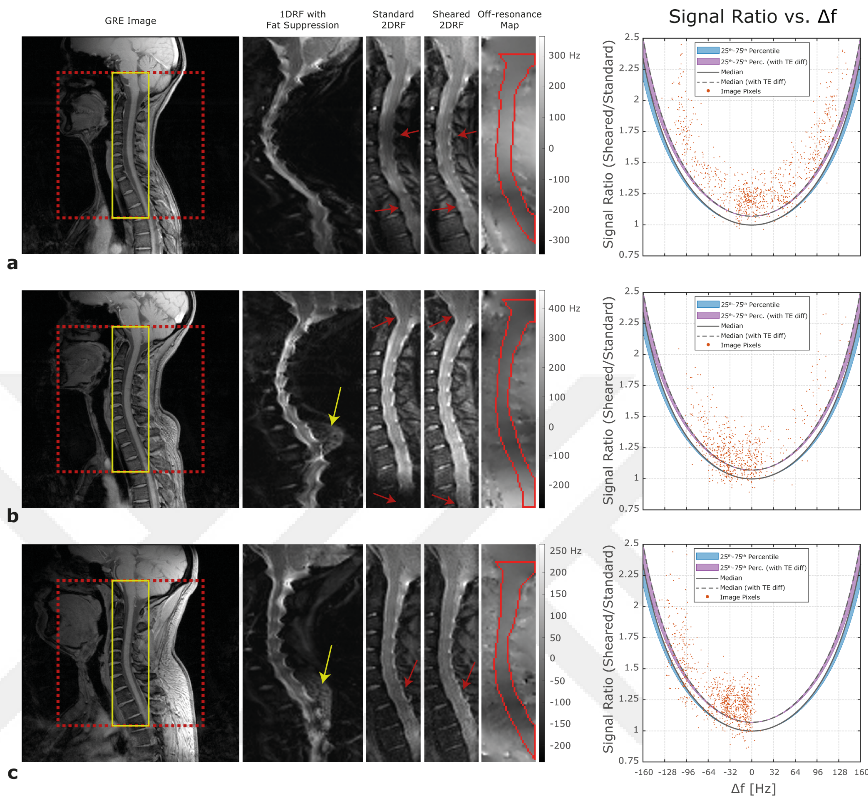

Figure 3.10: *In vivo imaging results in the cervical spine for all subjects. (a) Subject 1, (b) Subject 2, and (c) Subject 3. The images from the double-echo GRE sequences show the anatomy together with the full-FOV (red dashed rectangle) and reduced-FOV (yellow rectangle) regions marked for reference. The full-FOV images for all subjects (cropped versions shown), acquired using a 1D RF pulse with additional frequency-selective fat suppression, suffer from severe in-plane off-resonance distortions. Displaced fat signals overlap with and obscure the spinal cord in the lower cervical spine region for Subjects 2 and 3 (yellow arrows), indicating that fat suppression has failed for these subjects. In contrast, both the standard and sheared 2D RF pulses demonstrate high fidelity fat suppression, as well as high image resolution and reduced in-plane distortions. The sheared 2D RF pulse achieves visible signal improvement over the standard 2D RF pulse, especially in regions that suffer from high off-resonance (red arrows). The signal levels of the images obtained from the sheared and standard 2D RF pulses were compared quantitatively using the pixels within manually drawn ROIs covering the spinal cord (solid red lines in the off-resonance maps). The experimental signal ratio matches closely with the theoretical signal ratio (plotted with and without the TE difference taken into account) for all three subjects. These results confirm the signal improvement achieved via the off-resonance robustness of the sheared 2D RF design.*

Chapter 4

Sheared 2D RF Excitation for Reduced FOV Imaging on Low-Cost MRI Systems

This chapter is based on the publication titled "Barlas BA, Saritas EU. Making reduced FOV imaging applicable on low-cost MRI systems: A sheared 2DRF excitation approach". In the Proceeding of the 30th Annual Meeting of ISMRM, London, England, United Kingdom, 2022. p.2930.

4.1 Motivation

Although the advances in high-field MRI systems achieved high-quality images, installation and maintenance of these systems can be costly and complex, preventing wide accessibility to these systems [5, 50, 51, 52, 53]. Recently, relatively low-cost low-field MRI systems with laudable image quality have been introduced as cheaper alternatives to the high-field systems [5, 50, 54]. However, hardware limitations of these low-cost systems continue to be a major inconvenience, preventing the applicability of numerous popular MRI techniques [5, 50, 51]. As shown, the proposed sheared 2D RF excitation significantly improved the off-resonance robustness capability of reduced-FOV imaging on a 3 T MRI environment. In this chapter, sheared 2D RF design is proposed to make reduced-FOV imaging applicable on low-cost MRI systems, due to its pulse duration reduction capability. The proof-of-concept applicability of the proposed design is demonstrated for low-cost 0.35 T and 1.5 T MRI scanners via extensive simulations and phantom experiments in a custom head and neck phantom.

4.2 Methods

2D RF pulses were designed with the following hardware limits: $G_{\max} = 24$ mT/m and $S_{\max} = 55$ mT/m/ms for the 0.35 T MRI system, and $G_{\max} = 25$ mT/m and $S_{\max} = 90$ mT/m/ms for the 1.5 T MRI system. Again, both RF and gradient waveforms were designed using 2 μs sampling time.

Standard 2D RF pulses with blipped axis along the SS-direction were designed with the following design parameters: $FOV_{PE} = 40$ mm, $TBW_{PE} = 8$, $\Delta z = 4$ mm, $TBW_{SS} = 3$, and $N_{\max} = 16$ for both systems. The designed standard 2DRF pulses had 25.6 ms and 20.2 ms pulse durations for 0.35 T and 1.5 T MRI systems, respectively. For each standard 2D RF pulse, sheared 2DRF pulses with θ ranging between 30°-85° were generated such that N_{blip} was minimized under the unlimited slice coverage criterion in Eq 3.8 at each θ. Then, VERSE was utilized to obtain the waveforms with minimum pulse duration within the corresponding hardware limits [47].

Fat profiles were simulated with $\Delta f = 51$ Hz for 0.35 T, and $\Delta f = 220$ Hz for 1.5 T. For all simulations, T_1/T_2 relaxation effects were ignored when simulating the excitation profiles.

Next, effective 2D excitation profiles of all 2D RF pulses were simulated using Bloch simulations. Again, a subsequent 180° refocusing RF pulse with 2.34 ms pulse duration was utilized for this purpose. In this thesis, the total water signal of the target slice, total fat signal and total sidelobe signal (i.e., the total unsuppressed signal of the replicas after refocusing) were used as performance metrics and computed as a function of θ. For both systems, the best performing sheared 2D RF pulses were selected to minimize pulse durations while completely suppressing the sidelobe signal. Furthermore, sheared 2D RF pulses with relatively favorable fat suppression were selected to provide an alternative in terms of design requirements. Then, the mainlobe signals of the best performing sheared 2D RF pulses were compared with their standard counterparts under B_0 field inhomogeneities.

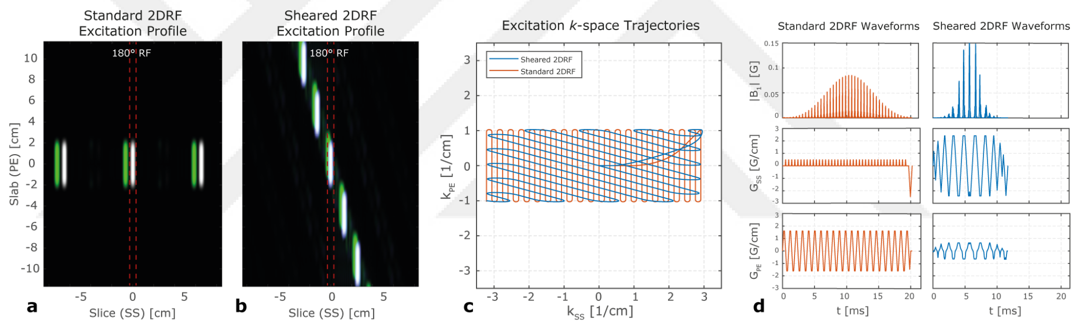

Figure 4.1: *2D excitation profiles (white for water and green for fat) for (a) the standard 2D RF pulse and (b) 75° sheared 2D RF pulse under 1.5 T hardware limitations. (c) Excitation k-space trajectories and (d) RF and gradient waveforms for the standard and sheared 2D RF pulses. The standard and sheared 2D RF pulses had 20.2 ms and 11.7 ms pulse durations, respectively, implying that the sheared 2D RF pulse achieves identical k-space coverage with considerably reduced pulse durations. For both 2D RF pulses, the design parameters were $FOV_{PE} = 40$ mm, $\Delta z = 4$ mm, $TBW_{SS} = 3$, and $TBW_{PE} = 8$. For the standard 2D RF pulse, $N_{\max} = 16$. The 2D RF pulses were designed under $G_{\max} = 25$ mT/m and $S_{\max} = 90$ mT/m/ms hardware limits.*

The above-mentioned hardware limits were emulated experimentally, by enforcing them on a 3 T MRI scanner (Siemens Magnetom Trio). The phantom experiments were performed using a custom 1:1 scale agar-agar brain and neck phantom [48]. For these experiments, sheared 2D RF pulse with $\theta = 75°$ for 0.35 T and sheared 2D RF pulses with $\theta = 56°$ and $\theta = 75°$ for 1.5 T were utilized. Furthermore, full-FOV imaging results were obtained together with the off-resonance field maps for both the 0.35 T and 1.5 T hardware limits. T2-weighted full-FOV ssEPI images were acquired using a standard 3 ms 1D RF pulse with 200×162.5 mm^2 full-FOV, 128×104 acquisition matrix, $TE = 77$ ms and $TE = 60$ ms for the 0.35 T and 1.5 T hardware limits, respectively. T2-weighted reduced-FOV ssEPI images were acquired using the sheared 2DRF pulses with 200×50 mm^2 reduced-FOV, 128×32 acquisition matrix. $TE = 31$ ms for the sheared 2D RF pulse designed with 0.35 T limits and $\theta = 75°$, $TE = 30$ ms for the sheared 2D RF pulse designed with 1.5 T limits and $\theta = 56°$, and $TE = 25$ ms for the sheared 2D RF pulse designed with 1.5 T limits and $\theta = 75°$. The common parameters were $\Delta z = 4$ mm, 6/8 partial Fourier acquisition, $TR = 6500$ ms, $BW = 1563$ Hz/pixel and $BW = 1628$ Hz/pixel for 0.35 T and 1.5 T, respectively. The off-resonance maps were obtained from the phase maps with the same procedure described in Section 3.2.3 MRI Experiments. Lastly, the pixel-wise signal ratios for the reduced-FOV images from the standard and sheared 2D RF cases were computed and plotted as a function of Δf at the corresponding pixels together with the theoretical expectation.

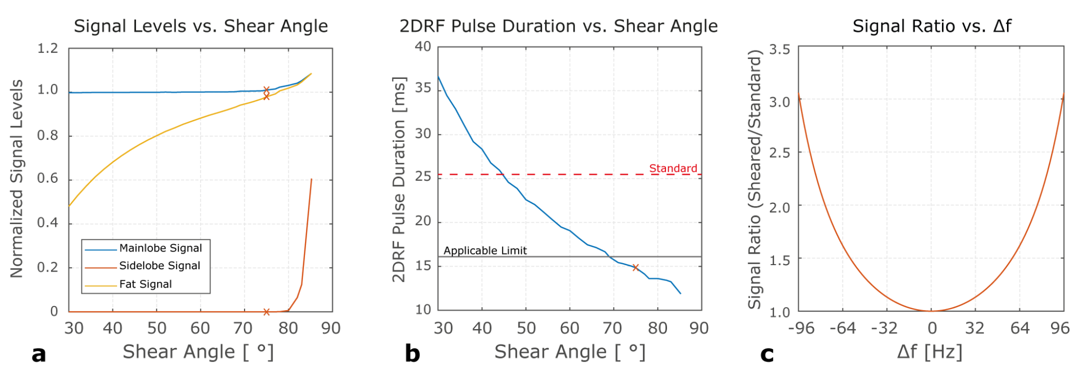

Figure 4.2: *Simulation results for 0.35 T MRI system. (a) Effective mainlobe, sidelobe, and fat signals as a function of θ. (b) The standard and sheared 2D RF pulse durations as a function of θ. $\theta = 75°$ (red cross) provides the shortest pulse duration with robust sidelobe suppression. (c) Signal ratio of the standard and 75° sheared 2D RF pulses under off-resonance in the range of -96 Hz to 96 Hz. The sheared 2D RF pulse achieves increased signal improvement under increased off-resonance, showing the improvements of shearing for low-cost MRI systems with high B_0 field inhomogeneities.*

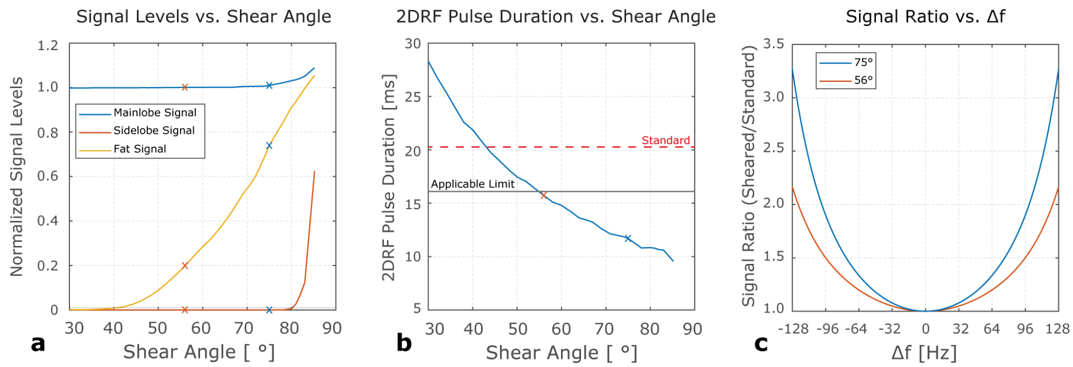

Figure 4.3: *Simulation results for 1.5 T MRI system. (a) Effective mainlobe, sidelobe, and fat signals as a function of θ. (b) The standard and sheared 2D RF pulse durations as a function of θ. Again, $\theta = 75°$ (blue cross) provides the shortest pulse duration with robust sidelobe suppression while $\theta = 56°$ (red cross) is an alternative with favorable fat suppression performance at the expense of increased pulse duration. (c) Signal ratio of the standard and the sheared 2D RF pulses under off-resonance in the range of -128 Hz to 128 Hz.*

4.3 Results

In Fig. 4.1, the 2D excitation profiles, k-space trajectories, and pulse waveforms of the standard and 75° sheared 2D RF pulses for 1.5 T hardware limits are shown. The sheared 2D RF pulse has significantly shorter duration than its standard counterpart, while providing the same k-space coverage. Note that the reduced duration of the sheared 2D RF pulse also decreased the separation between the water and fat profiles, limiting the fat suppression capability for this case.

Figures 4.2-4.3 show the effective mainlobe, sidelobe, and fat signals together with pulse durations as a function of θ under 0.35 T and 1.5 T hardware limits, respectively. The standard 2D RF pulses had 25.6 ms and 20.2 ms pulse durations for 0.35 T and 1.5 T MRI systems, respectively, exceeding the applicable duration limits of MRI scanners (16 ms for the utilized MRI scanner). For both systems, the sheared 2D RF pulse duration decreases with increasing θ. The sidelobe signal demonstrates reliable suppression until $\theta = 79°$, while it exponentially increases for $\theta \geq 79°$. However, an increase in θ almost linearly increases unsuppressed fat signal, indicating that additional fat suppression may be required at high θ especially for systems with small B_0 field (0.35 T in this case). To minimize the pulse duration while preserving robust sidelobe suppression, the optimal sheared 2D RF pulses were chosen as $\theta = 75°$ for 0.35 T and $\theta = 75°$ for 1.5 T, with the durations 14.8 ms and 11.7 ms, respectively. In addition, $\theta = 56°$ for 1.5 T was chosen as an alternative design with favorable fat suppression, albeit with a longer duration of 15.7 ms. As shown in Fig. 4.2c-4.3c, the sheared 2D RF pulses achieve improved signal levels under off-resonance effects compared to their standard counterparts, which is especially advantageous for the low-cost MRI systems suffering from high B_0 inhomogeneities.

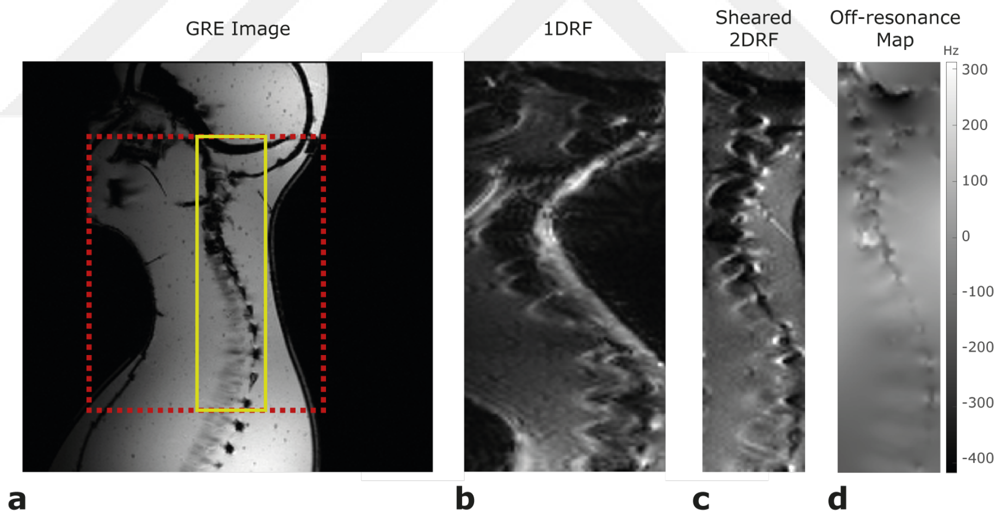

Figure 4.4: *Phantom imaging results at 0.35 T hardware limits. (a) GRE image indicating full-FOV ROI (red dashed line) with 200×162.5 mm^2 and reduced-FOV ROI (yellow line) with 200×50 mm^2. (b) Full-FOV image suffers severely from in-plane off-resonance effects, while (c) the reduced-FOV image using sheared 2D RF pulse successfully alleviates these artifacts. (d) Off-resonance map for the reduced-FOV ROI. The hardware limits of $G_{\max} = 24$ mT/m and $S_{\max} = 55$ mT/m/ms were emulated by enforcing them on a 3 T MRI scanner (Siemens Magnetom Trio).*

Figures 4.4-4.5 show phantom imaging results at 0.35 T and 1.5 T hardware limits, respectively. Full-FOV images suffer severely from in-plane off-resonance effects especially for 0.35 T, while reduced-FOV images with the sheared 2D RF pulses successfully alleviate these artifacts. For 1.5 T, 75° sheared 2D RF pulse further improves the signal level with respect to 56° sheared 2D RF pulse. This result is verified in Fig. 4.5f by the pixel-wise signal comparison of the reduced-FOV images for 75° and 56°, where the experimental and theoretical signal ratios closely follow each other. The signal improvement with respect to the standard 2D RF pulses could not be verified experimentally, as the standard 2D RF pulses were not applicable due to their long pulse durations. However, the results in Fig. 4.5f indicate the validity of the signal improvements predicted in Fig. 4.2-4.3 by showing that reduced pulse durations provide off-resonance robustness due to their increased BW_{SS}.

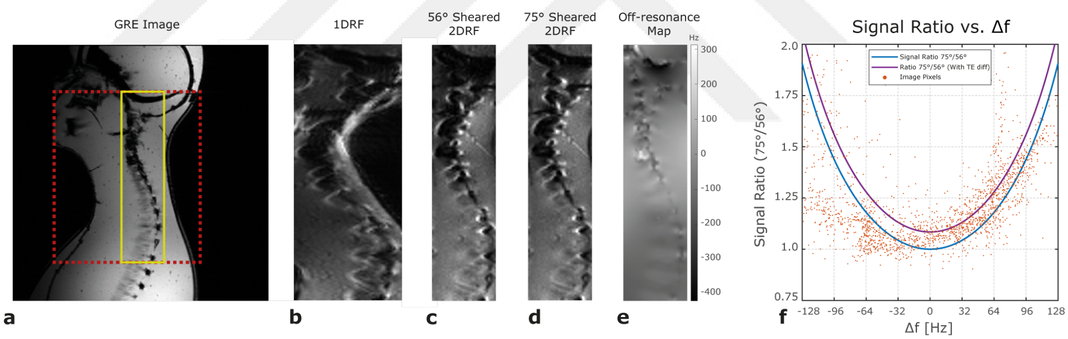

Figure 4.5: *Phantom imaging results at 1.5 T hardware limits. (a) GRE image showing full-FOV ROI (red dashed line) with* 200×162.5 *mm*^{2} *and reduced-FOV ROI (yellow line) with* 200×50 *mm*^{2}*. (b) Full-FOV image suffers from in-plane off-resonance effects, while (c-d) the reduced-FOV images obtained using sheared 2DRF pulses with* $\theta = 56°$ *and* $\theta = 75°$ *remove these artifacts. (e) Off-resonance map for the reduced-FOV ROI. (f) Pixel-wise signal ratio of the reduced-FOV images. The experimental signal ratio closely follows the theoretical signal ratio curve. The hardware limits of* $G_{\max} = 25$ *mT/m and* $S_{\max} = 90$ *mT/m/ms were emulated by enforcing them on a 3 T MRI scanner (Siemens Magnetom Trio).*

Chapter 5

Discussion and Conclusion

In this thesis, a sheared 2D RF pulse design that significantly reduces pulse durations and provides robustness against through-plane off-resonance effects, while eliminating slice coverage limitations was proposed. Increasing the shear angle θ enables a reduction in the number of lines needed to cover the excitation k-space, which in turn reduces the pulse durations drastically while preserving the sharpness of the 2D excitation profile. According to Eq. 2.6, the resulting increase in bandwidth decreases the separation between water and fat profiles, which may jeopardize fat suppression capability. Since unsuppressed fat signal experiences a large in-plane displacement in ssEPI sequences, inherent fat suppression is a highly desirable feature. Here, a target fat/water signal ratio of 5% was chosen as a design criterion, and the robustness of this approach was verified with reliable fat suppression demonstrated for in vivo imaging in the cervical spinal cord (see Fig. 3.10).

The simulation results in Fig. 3.5 confirm that the sheared 2D RF can successfully shorten the pulse duration for a wide range of design parameters, and that it becomes increasingly advantageous over the standard design as TBW_{PE} increases and FOV_{PE} decreases. This scenario corresponds to the case of a sharp slab profile over a small FOV_{PE}, i.e., the typical scenario targeted with reduced-FOV applications. Furthermore, the sheared 2D RF design is highly effective in reducing pulse durations for typical hardware limits, and it becomes especially beneficial at reduced $S_{\max}$. It should be noted that even for the cases where the reduction in pulse duration is relatively small, the sheared design still holds the advantage of providing unlimited slice coverage, while preserving the fat suppression capability.

The through-plane off-resonance robustness achieved by the sheared 2D RF design was successfully demonstrated through extensive simulations, phantom experiments, and in vivo imaging experiments in the cervical spinal cord. The experimental results demonstrated a slightly higher signal ratio than expected, even after taking the TE difference into account. Here, T_1/T_2 relaxation during RF pulses were ignored during theoretical computations. Therefore, the increased signal ratio in the experiments may reflect the added advantage of reduced relaxation effects for the sheared 2D RF pulse due to its shorter duration. In addition, signal pileup artifacts may also be a potential source, as multiple pixels experiencing different off-resonance frequencies may pile-up on to the same pixel in ssEPI images, making it difficult to resolve the true pixel intensities. Lastly, noise or deviations from the assumed T_2 value (especially for the in vivo case) may also be contributing factors to the observed variations.

The imaging experiments in this thesis were performed with the goal of highlighting the off-resonance robustness achieved via the sheared 2D RF design. The relatively large FOV in the sagittal plane and the large susceptibility differences around the cervical spine provided a suitable environment for this goal. Off-resonance frequencies reaching well above 128 Hz ($>$ 1 ppm) were observed, enabling experimental verification of the signal improvement achieved via the sheared design. In practice, imaging the spinal cord in the sagittal plane may complicate slice prescription, requiring oblique sagittal imaging. With that said, the axial plane is generally preferred for spinal cord imaging, as it can better resolve the fiber bundles in the cord [55]. However, imaging the spine in the axial plane requires a large number of slices, easily exceeding $N_{\max}$ of a standard 2D RF pulse [24]. For those cases, the standard 2D RF pulse will experience partial saturation effects, causing the signal ratio to further increase in favor of the sheared 2D RF pulse. Note that if $N_{\max}$ is exceeded, the fat profile of the standard 2D RF pulse would also experience partial saturation. However, because fat is already completely suppressed after the 180° RF pulse, partial saturation does not affect the fat signal. For the sheared 2D RF pulse, the replicas of the fat profile are shifted along the sheared axis with identical separation as that of the water profile replicas (see Fig. 3.2b). Therefore, no partial saturation effect occurs for the sheared 2D RF pulse during multislice imaging.

Both the sheared and the standard 2D RF pulses were designed under identical hardware constraints and were optimized for minimal pulse duration. For the example shown in Fig. 3.1, the reduction in pulse duration at a fixed flip angle caused the peak B_1 to increase from 10 μT to 15 μT for the sheared design. While 15 μT peak B_1 is within the hardware limits for MRI scanners, the specific absorption rate (SAR) for the sheared 2D RF pulse is 64% higher than its standard counterpart for this case. As a reference, the default excitation of the stock ssEPI sequence contained a standard 1D RF pulse with a peak B_1 of 7.2 μT preceded by a frequency-selective fat suppression RF pulse with a peak B_1 of 2.9 μT. When compared to this default excitation, the SAR of the sheared 2D RF pulse was 22% higher, whereas that of the standard 2D RF pulse was 26% lower. Considering the in-plane and through-plane off-resonance robustness provided by the sheared 2D RF pulse, the slight increase in SAR is tolerable. Note that the reported SAR values are highly dependent on the pulse durations (and hence the peak B_1 and gradient limits), as well as the specific design parameters for the 2D RF pulse. In the cases where the sheared design is more effective in reducing pulse durations (e.g., at reduced $S_{\max}$), the relative increase in SAR with respect to the standard 2D RF pulse will become more significant. Nonetheless, since ssEPI sequences utilize long TRs (typically TR ¿ 3000 ms), the increase in SAR for the sheared 2D RF pulse is not expected to be a limiting factor.

The proposed sheared 2D RF pulse features a common design goal as that of the tilted 2D RF pulse [24]: positioning the replicas outside the slice stack to provide unlimited slice coverage. Because rotation and shearing are fundamentally different operations, the angle θ that guarantees unlimited slice coverage is different for the two cases: the equation for the tilt angle θ has an arcsine relation, whereas the shear angle θ has an arctangent relation with respect to the same parameters. The tilted design rotates the k-space trajectory by the tilt angle θ, without altering N_{blip} or Δk_{SS}. As a result, the tilted design does not achieve any pulse duration reduction and has minimal off-resonance robustness advantage over the standard 2D RF pulse [24]. Furthermore, rotation causes poor coverage of the targeted k-space extent, causing degradation in 2D profile quality. In contrast, the sheared 2D RF design minimizes N_{blip} and maximizes Δk_{SS} for a given shear angle θ, achieving significant reductions in the pulse duration. Note that one could decrease N_{blip} and increase Δk_{SS} to reduce the tilted 2D RF pulse duration, as well. However, making N_{blip} smaller would cause the tilt angle θ to increase, which would further exacerbate the poor k-space coverage problem, causing severe degradations in the 2D profile. A related work proposed starting from a square echo-planar trajectory, followed by rotation and scaling to better cover a rectangular k-space extent [56]. While the resulting tilted trajectory overcame some of the aforementioned poor k-space coverage issues, it still did not cover the entirety of the targeted k-space extent and hence is prone to 2D profile degradations. In contrast, even direct shearing of the trajectory provides good coverage of the targeted k-space. The proposed tailoring of the sheared trajectory achieves identical coverage as the standard trajectory, preserving 2D profile quality. While the standard 2D RF pulse duration could also be reduced by decreasing N_{blip}, doing so would increase partial saturation effects during multislice acquisitions. Alternatively, N_{blip} and TBW_{SS} could be decreased at the same rate to keep $N_{\max}$ constant, which in turn would degrade the slice profile. Nonetheless, the sheared design can provide further reduction in pulse durations even for small TBW_{SS} cases (see Fig. 3.5b), with the added advantage of unlimited slice coverage. Moreover, Fig. 3.5 demonstrates that the sheared design also provides a flexibility while choosing θ for a given 2D profile. Consequently, pulse durations could be further shortened by increasing θ, forsaking the fat suppression performance in favor of further improvement in off-resonance robustness. In such a case, an external fat suppression method can be incorporated, such as a frequency-selective fat suppression RF pulse or a short tau inversion recovery (STIR).

The efficacy of the sheared 2D RF design is further investigated for the low-cost low-field MRI systems, where the standard 2D RF pulses are not applicable due to their hardware limitation, by making reduced-FOV imaging applicable for these systems. Analogous to the results shown in Fig. 3.5c, Fig. 4.2b shows that sheared 2D RF design excels for the given 0.35 T MRI system, where $S_{\max} = 90$ mT/m/ms, in terms of its capability to reduce pulse durations and off-resonance robustness. As shown in Fig. 3.5c and Fig. 4.3b, the performance of the sheared design for the 1.5 T MRI system, where $S_{\max} = 55$ mT/m/ms, is similar to the lower $S_{\max}$ case (i.e., $S_{\max} = 100$ mT/m/ms), implying the consistency of the sheared 2D RF pulse across various MRI systems. Furthermore, this significant reduction in the pulse duration enables considerable improvement in the off-resonance robustness even for small Δf which is especially beneficial for low-cost MRI systems with high B_0 field inhomogenieties as shown in Fig. 4.2b-4.3b. However, sheared 2D RF design loses its fat suppression capability in lower fields due to the reduced chemical shifts. Still, an external fat suppression technique could be integrated for these systems, allowing complete fat suppression. Note that fat suppression is also essential for full-FOV imaging with ssEPI due to the long T_{esp} of the EPI trajectory.

In this thesis, the blipped direction for the standard 2D RF pulse was the SS-axis. An alternative design is to assign the PE-axis as the blipped direction [29], which requires large N_{blip} or small TBW_{PE} to prevent aliasing artifacts due to the replicas along the PE-direction. Note that aliasing is a considerably more severe problem than the above-mentioned signal loss due to partial saturation effect. To avoid aliasing, a tilted alternative was proposed to rotate the k-space trajectory by a relatively small tilt angle θ, such that a subsequent 180° RF pulse can suppress the replicas [37]. However, both the original and tilted designs require additional fat suppression and have reduced slab sharpness due to the need for small TBW_{PE}, an undesirable feature for reduced-FOV imaging. Another alternative approach for reduced-FOV imaging is to utilize 2D spatially selective excitation with a spiral trajectory [44], which provides relatively short pulse durations especially after applying a variable slew-rate spiral trajectory [57]. However, spiral RF pulse is more suited for circular 2D excitation profiles, as it lacks the flexibility of independent design along the SS- and PE-axis. In contrast, the proposed sheared 2D RF pulse provides sharp slab and slice profiles, with unlimited slice coverage and inherent fat suppression capability.

To summarize, this thesis proposed a sheared 2D RF pulse design to achieve robustness against through-plane off-resonance effects via a significant reduction in pulse duration. This technique eliminates slice coverage limitations, while maintaining profile sharpness and high fidelity fat suppression. The performance of the proposed technique was demonstrated in the cervical spine, showing significant signal improvements in regions exposed to off-resonance effects. While the results were demonstrated for ssEPI images, this design can be applied for reduced-FOV imaging for spin echo sequences with any acquisition type. The proposed sheared 2D RF approach will be especially beneficial in regions that suffer from large off-resonance effects, such as spinal cord and breast.

Bibliography

[1] S. Reeder and P. Mujherjee, "Clinical applications of MR diffusion and perfusion imaging," *Magn Reson Imaging Clin N Am*, vol. 17, pp. xi–xii, 2009.

[2] S. Holdsworth, R. O'Halloran, and K. Setsompop, "The quest for high spatial resolution diffusion-weighted imaging of the human brain in vivo," *NMR Biomed*, vol. 32, no. 4, p. e4056, 2019.

[3] M. Brazzelli, P. Sandercock, F. Chappell, M. Celani, E. Righetti, N. Arestis, J. Wardlaw, and J. Deeks, "Magnetic resonance imaging versus computed tomography for detection of acute vascular lesions in patients presenting with stroke symptoms," *Cochrane Database Syst Rev*, vol. 7, no. 4, 2009.

[4] J. Barentsz, J. Richenberg, R. Clements, P. Choyke, S. Verma, G. Villeirs, O. Rouviere, V. Logager, and J. Fütterer, "ESUR prostate MR guidelines 2012," *Eur Radiol*, vol. 22, pp. 746–757, 2012.

[5] S. Bhat, T. Fernandes, P. Poojar, S. F. M. da, P. Rao, M. Hanumantharaju, G. Ogbole, R. Nunes, and S. Geethanath, "Low-Field MRI of stroke: challenges and opportunities," *J Magn Reson Imaging*, vol. 54, no. 2, pp. 372–390, 2021.

[6] G. Zaharchuk, E. Saritas, J. Andre, C. Chin, J. Rosenberg, T. Brosnan, A. Shankaranarayan, D. Nishimura, and N. Fischbein, "Reduced field-of-view diffusion imaging of the human spinal cord: comparison with conventional single-shot echo-planar imaging," *AJNR Am J Neuroradiol*, vol. 32, no. 5, pp. 813–820, 2011.

[7] O. Dietrich, A. Biffar, A. Baur-Melnyk, and M. Reiser, "Technical aspects of MR diffusion imaging of the body," *Eur J Radiol*, vol. 76, no. 3, pp. 314–322, 2010.

[8] L. Singer, L. Wilmes, E. Saritas, A. Shankaranarayanan, E. Proctor, D. Wisner, B. Chang, B. Joe, D. Nishimura, and N. Hylton, "High-resolution diffusion-weighted magnetic resonance imaging in patients with locally advanced breast cancer," *Acad Radiol*, vol. 19, no. 5, pp. 526–534, 2012.

[9] N. Korn, J. Kurhanewicz, S. Banerjee, O. Starobinets, E. Saritas, and S. Noworolski, "Reduced-FOV excitation decreases susceptibility artifact in diffusion-weighted MRI with endorectal coil for prostate cancer detection," *Magn Reson Imaging*, vol. 33, no. 1, pp. 56–62, 2015.

[10] S. Leibfarth, R. Winter, H. Lyng, D. Zips, and D. Thorwarth, "Potentials and challenges of diffusion-weighted magnetic resonance imaging in radiotherapy," *Clin Transl Radiat Oncol*, vol. 13, pp. 29–37, 2018.

[11] H. An, X. Ma, Z. Pan, H. Guo, and E. Lee, "Qualitative and quantitative comparison of image quality between single-shot echo-planar and interleaved multi-shot echo-planar diffusion-weighted imaging in female pelvis," *Eur Radiol*, vol. 30, no. 4, pp. 1876–1884, 2020.

[12] J. Tournier, S. Mori, and A. Leemans, "Diffusion tensor imaging and beyond," *Magn Reson Med*, vol. 65, no. 6, pp. 1532–1556, 2011.

[13] S. Holdsworth, S. Skare, R. Newbould, R. Guzmann, N. Blevins, and R. Bammer, "Readout-segmented EPI for rapid high resolution diffusion imaging at 3 T," *Eur J Radiol*, vol. 65, no. 1, pp. 36–46, 2008.

[14] S. Holdsworth, S. Skare, R. Newbould, and R. Bammer, "Robust GRAPPA-accelerated diffusion-weighted readout-segmented (RS)-EPI," *Magn Reson Med*, vol. 62, no. 6, pp. 1629–1640, 2009.

[15] R. Heidemann, D. Porter, A. Anwander, K. H. T Feiweier, T. Knösche, and R. Turner, "Diffusion imaging in humans at 7T using readout-segmented EPI and GRAPPA," *Magn Reson Med*, vol. 64, no. 1, pp. 9–14, 2010.

[16] S. Skare, R. Newbould, A. Nordell, S. Holdsworth, and R. Bammer, "An auto-calibrated, angularly continuous, two-dimensional GRAPPA kernel for propeller trajectories," *Magn Reson Med*, vol. 60, no. 6, pp. 1457–1465, 2008.

[17] K. Butts, A. de Crespigny, J. Pauly, and M. Moseley, "Diffusion-weighted interleaved echo-planar imaging with a pair of orthogonal navigator echoes," *Magn Reson Med*, vol. 35, no. 5, pp. 763–770, 1996.

[18] S. Guhaniyogi, M. Chu, H. Chang, A. Song, and N. Chen, "Motion immune diffusion imaging using augmented MUSE for high-resolution multi-shot EPI," *Magn Reson Med*, vol. 75, no. 2, pp. 639–652, 2016.

[19] W. Liu, X. Zhao, Y. Ma, X. Tang, and J. Gao, "DWI using navigated interleaved multishot EPI with realigned GRAPPA reconstruction," *Magn Reson Med*, vol. 75, no. 1, pp. 280–286, 2016.

[20] Z. Dong, F. Wang, X. Ma, Z. Zhang, E. Dai, C. Yuan, and H. Guo, "Interleaved EPI diffusion imaging using SPIRiT-based reconstruction with virtual coil compression," *Magn Reson Med*, vol. 79, no. 3, pp. 1525–1531, 2018.

[21] D. Feinberg, J. Hoenninger, L. Crooks, L. Kaufman, J. Watts, and M. Arakawa, "Inner volume MR imaging: technical concepts and their application," *Radiology*, vol. 156, no. 3, pp. 743–747, 1985.

[22] B. Wilm, J. Svensson, A. Henning, K. Pruessmann, P. Boesiger, and S. Kollias, "Reduced field-of-view MRI using outer volume suppression for spinal cord diffusion imaging," *Magn Reson Med*, vol. 57, no. 3, pp. 625–630, 2007.

[23] E. Saritas, C. Cunningham, J. Lee, E. Han, and D. Nishimura, "DWI of the spinal cord with reduced FOV single-shot EPI," *Magn Reson Med*, vol. 60, no. 2, pp. 468–473, 2008.

[24] S. Banerjee, D. Nishimura, A. Shankaranarayanan, and E. Saritas, "Reduced field-of-view DWI with robust fat suppression and unrestricted slice coverage using tilted 2D RF excitation," *Magn Reson Med*, vol. 76, no. 6, pp. 1668–1676, 2016.

[25] R. Heidemann, A. Anwander, T. Feiweier, T. Knösche, and R. Turner, "k-space and q-space: combining ultra-high spatial and angular resolution in diffusion imaging using ZOOPPA at 7 T.," *Neuroimage*, vol. 60, no. 2, pp. 967–978, 2012.

[26] C. Wargo and J. Gore, "Localized high-resolution DTI of the human midbrain using single-shot EPI, parallel imaging, and outer-volume suppression at 7T," *Magn Reson Imaging*, vol. 31, no. 6, pp. 810–819, 2013.

[27] C. Wheeler-Kingshott, S. Hickman, G. Parker, O. Ciccarelli, M. Symms, D. Miller, and G. Barker, "Investigating cervical spinal cord structure using axial diffusion tensor imaging," *Neuroimage*, vol. 16, no. 1, pp. 93–102, 2002.

[28] N. Dowell, T. Jenkins, O. Ciccarelli, D. Miller, and C. Wheeler-Kingshott, "Contiguous-slice zonally oblique multislice (CO-ZOOM) diffusion tensor imaging: examples of in vivo spinal cord and optic nerve applications," *Magn Reson Imaging*, vol. 29, no. 2, pp. 454–460, 2009.

[29] J. Finsterbusch, "High-resolution diffusion tensor imaging with inner field-of-view EPI," *J Magn Reson Imaging*, vol. 29, no. 4, pp. 987–993, 2009.

[30] B. Wilm, U. Gamper, A. Henning, K. Pruessmann, S. Kollias, and P. Boesiger, "Diffusion-weighted imaging of the entire spinal cord," *NMR Biomed*, vol. 22, no. 2, pp. 174–181, 2009.

[31] J. Andre, G. Zaharchuk, E. Saritas, S. Komakula, A. Shankaranarayan, S. Banerjee, J. Rosenberg, D. Nishimura, and N. Fischbein, "Clinical evaluation of reduced field-of-view diffusion-weighted imaging of the cervical and thoracic spine and spinal cord," *AJNR Am J Neuroradiol*, vol. 33, no. 10, pp. 1860–1866, 2012.

[32] L. Wilmes, R. McLaughlin, D. Newitt, L. Singer, S. Sinha, E. Proctor, D. Wisner, E. Saritas, J. Kornak, A. Shankaranarayanan, S. Banerjee, E. Jones, B. Joe, and N. Hylton, "High-resolution diffusion-weighted imaging for monitoring breast cancer treatment response," *Acad Radiol*, vol. 20, no. 5, pp. 581–589, 2013.

[33] Y. Zhang, J. Holmes, I. Rabanillo, A. Guidon, S. Wells, and D. Hernando, "Quantitative diffusion MRI using reduced field-of-view and multi-shot acquisition techniques: Validation in phantoms and prostate imaging," *Magn Reson Imaging*, vol. 51, pp. 173–181, 2018.

[34] R. Schneider, D. Ritter, J. Haueisen, and J. Pfeuffer, "B0-informed variable density trajectory design for enhanced correction of off-resonance effects in parallel transmission," *Magn Reson Med*, vol. 71, no. 4, pp. 1381–1393, 2014.

[35] C. Ma, D. Xu, K. King, and Z. Liang, "Reduced field-of-view excitation using second-order gradients and spatial-spectral radiofrequency pulses," *Magn Reson Med*, vol. 69, no. 2, pp. 503–508, 2013.

[36] H. Islam and G. Glover, "Reduced field of view imaging using a static second-order gradient for functional MRI applications," *Magn Reson Med*, vol. 75, no. 2, pp. 817–822, 2016.

[37] J. Finsterbusch, "Improving the performance of diffusion-weighted inner field-of-view echo-planar imaging based on 2D-selective radiofrequency excitations by tilting the excitation plane," *J Magn Reson Imaging*, vol. 35, no. 4, pp. 984–992, 2012.

[38] E. Lee, J. Hwang, Y. Chang, S. Hong, E. Oh, B. Nam, J. Sung, and B. Thomas, "Modified reduced field-of-view diffusion-weighted magnetic resonance imaging of the prostate: comparison with reduced field-of-view imaging and single shot echo-planar imaging," *J Comput Assist Tomogr*, vol. 45, no. 3, pp. 367–373, 2021.

[39] M. Tanabe, M. Higashi, T. Benkert, H. Imai, K. Miyoshi, F. Kameda, S. Ariyoshi, K. Ihara, and K. Ito, "Reduced field-of-view diffusion-weighted magnetic resonance imaging of the pancreas with tilted excitation plane: A preliminary study," *J Magn Reson Imaging*, vol. 54, no. 3, pp. 715–720, 2021.

[40] D. LeBihan, J. Mangin, C. Poupon, C. Clark, S. Pappata, N. Molko, and H. Chabriat, "Diffusion tensor imaging: concepts and applications," *J Magn Reson Imaging*, vol. 13, no. 4, pp. 534–546, 2001.

[41] A. Anderson and J. Gore, "Analysis and correction of motion artifacts in diffusion weighted imaging," *Magn Reson Med*, vol. 32, no. 3, pp. 379–387, 1994.

[42] P. Jezzard and R. Balaban, "Correction for geometric distortion in echo planar images from B0 field variations," *Magn Reson Med*, vol. 34, no. 1, pp. 65–73, 1995.

[43] P. LeRoux, R. Gilles, G. McKinnon, and P. Carlier, "Optimized outer volume suppression for single-shot fast spin-echo cardiac imaging," *J Magn Reson Imaging*, vol. 8, no. 5, pp. 1022–1032, 1998.

[44] J. Pauly, D. Nishimura, and A. Macovski, "A k-space analysis of small-tip-angle excitation," *J Magn Reson*, vol. 81, no. 1, pp. 43–56, 1989.

[45] M. Alley, J. Pauly, F. Sommer, and N. Pelc, "Angiographic imaging with 2D RF pulses," *Magn Reson Med*, vol. 37, no. 2, pp. 260–267, 1997.

[46] S. Conolly, D. Nishimura, A. Macovski, and G. Glover, "Variable-rate selective excitation," *J Magn Reson*, vol. 78, no. 3, pp. 440–458, 1988.

[47] D. Lee, M. Lustig, W. Grissom, and J. Pauly, "Time-optimal design for multidimensional and parallel transmit variable-rate selective excitation," *Magn Reson Med*, vol. 61, no. 6, pp. 1471–1479, 2009.

[48] E. Aygun, R. Cagil, and E. Saritas, "1-1 scale agar-agar paramagnetic phantom for brain and cervical spine MRI," in *Proc. of the 2021 Annual Meeting of ISMRM*, p. 3355, 2021.

[49] S. Smith, R. Edden, J. Farrell, P. Barker, and P. V. Zijl, "Measurement of T_1 and T_2 in the cervical spinal cord at 3 tesla," *Magn Reson Med*, vol. 60, no. 1, pp. 213–219, 2008.

[50] J. Marques, F. Simonis, and A. Webb, "Low-field MRI: An MR physics perspective," *J Magn Reson Imaging*, vol. 49, no. 6, pp. 1528–1542, 2019.

[51] L. Wald, P. McDaniel, T. Witzel, J. Stockmann, and C. Cooley, "Low-cost and portable MRI," *J Magn Reson Imaging*, vol. 52, no. 3, pp. 686–696, 2020.

[52] W. H. Organization, "Global atlas of medical devices.," 2017.

[53] OECD, "Health equipment - Magnetic resonance imaging(MRI) units - OECD Data," 1999.

[54] A. Campbell-Washburn, R. Ramasawmy, M. Restivo, I. Bhattacharya, B. Basar, D. Herzka, M. Hansen, T. Rogers, W. Bandettini, D. McGuirt, C. Mancini, D. Grodzki, R. Schneider, W. Majeed, H. Bhat, H. Xue, J. Moss, A. Malayeri, E. Jones, A. Koretsky, P. Kellman, M. Chen, R. Lederman, and R. Balaban, "Opportunities in interventional and diagnostic imaging by using high-performance low-field-strength MRI," *Radiology*, vol. 293, no. 3, pp. 384–393, 2019.

[55] P. Stroman, C. Wheeler-Kingshott, M. Bacon, J. Schwab, R. Bosma, J. Brooks, D. Cadotte, T. Carlstedt, O. Ciccarelli, J. Cohen-Adad, A. Curt, N. Evangelou, M. Fehlings, M. Filippi, B. Kelley, S. Kollias, A. Mackay, C. Porro, S. Smith, S. Strittmatter, P. Summers, and I. Tracey, "The current state-of-art of spinal cord imaging: Methods," *Neuroimage*, vol. 84, pp. 1070–1081, 2014.

[56] Z. Zhong, D. Merkitch, M. Karaman, J. Zhang, Y. Sui, J. Goldman, and X. Zhou, "High-spatial-resolution diffusion MRI in Parkinson disease: Lateral asymmetry of the substantia nigra," *Radiology*, vol. 291, no. 1, pp. 149–157, 2019.

[57] D. Xu, K. King, and Z. Liang, "Variable slew-rate spiral design: Theory and application to peak B1 amplitude reduction in 2D RF pulse design," *Magn Reson Med*, vol. 58, no. 4, pp. 835–842, 2007.